A process-structure-property model via physics-based/data-driven hybrid methods for freeze-cast porous ceramics in Si3N4-Si2N2O case system

Xingqi Liao, Mingqing Liao, Chong Wei, Zhiheng Huang, Wenjiu Duan, Xiaoming Duan, Delong Cai, Laurent Gremillard, Zhihua Yang, Dechang Jia, et al.

A process-structure-property model via physics-based/data-driven hybrid methods for freeze-cast porous ceramics in Si_3N_4-Si_2N_2O case system

This article has been published in
Acta Materialia (2024) Vol. 169, 119819
https://doi.org/10.1016/j.actamat.2024.119819

Xingqi Liao[a,+], Mingqing Liao[a,f,+], Chong Wei[c,d], Zhiheng Huang[e], Wenjiu Duan[a,b,*], Xiaoming Duan[a], Delong Cai[a], Laurent Gremillard[d], Zhihua Yang[a,*], Dechang Jia[a], Yu Zhou[a]

[a] Institute for Advanced Ceramics, School of Materials Science and Engineering, Harbin Institute of Technology, Harbin 150080, China
[b] Tsinghua Shenzhen International Graduate School, Tsinghua University, Shenzhen 518055, China
[c] School of Mechanics, Civil Engineering and Architecture, Northwestern Polytechnical University, Xi'an 710072, China
[d] University of Lyon, INSA-Lyon, CNRS, MATEIS, UMR 5510, Villeurbanne F-69621, France
[e] School of Materials Science and Engineering, Sun Yat-sen University, Guangzhou 510006, China
[f] School of Materials Science and Engineering, Jiangsu University of Science and Technology, Zhenjiang 212100, China

[+] These authors contributed equally to this work
[*] Corresponding authors : dwenjiu@foxmail.com ; zhyang@hit.edu.cn

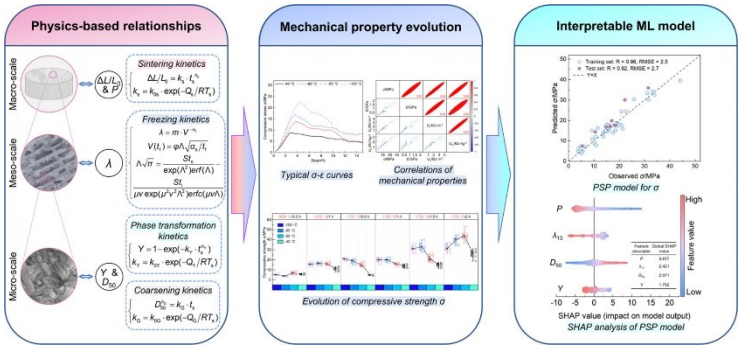

Abstract

For the engineering applications of freeze-cast porous ceramics, the demand targets are often multiple and competing, which is a challenging problem to seek a Nash equilibrium in the high-dimensional design space. An accurate and robust quantification of process-structure-property correlations would provide an effective path to find the set of Pareto optimal materials for one specific need. In this work, using porous Si_3N_4-Si_2N_2O ceramics as the model materials, a hybrid model for the quantitative design of the microstructure and mechanical properties is developed from four physics-based process-microstructure models with sintering, solidification, phase transformation and grain growth kinetic theories, and the subsequent data-driven structure-property model utilizing a machine learning method, artificial neural network (ANN). The SHapely Additive exPlanations (SHAP) analysis is further introduced to interpret the ANN model and mathematically identify the contribution of each microstructure feature descriptor toward target mechanical property outputs. These results present a systematic understanding of the process-structure-property relationships through the hybrid model, guiding the optimal design of the freeze-cast porous ceramics with required microstructures and mechanical properties.

Keywords

Freeze-casting; Porous ceramics ; Microstructures ; Kinetics ; Machine learning

1. Introduction

Porous ceramics, owing to their lightness, high-temperature resistance, chemical inertness, and biocompatibility, play an essential and multifunctional role in metallurgy, energy, biomedical, and other fields [1-7]. Since the first publications by T. Fukasawa *et al*. [8,9] in 2001, freeze-casting (also named ice-templating) porous ceramics with unidirectional pore configurations, as a unique member of the porous ceramic family, have been extensively studied [10,11]. The high open porosity, tunable pore structure, and properties derived from the longitudinally aligned structure of porous ceramics prepared by the well-established freeze-casting route enable widespread applications involving thermal insulation components, hot gas filters, catalyst supports, and tissue engineering scaffolds [10-15]. Especially, porous Si_3N_4 ceramics with excellent mechanical properties, good resistance to thermal shock, favorable biocompatibility and antibacterial property have great potential in the above applications [16-21]. In high-temperature oxidizing environments, Si_2N_2O, with the superior oxidation resistance, is a valuable addition for enhancing the performance of Si_3N_4-based ceramics, making the Si_3N_4-Si_2N_2O system garner widely attention and interest [22,23].

Tailoring materials towards specific needs remains the challenge in a multi-objective optimization issue with high-dimensional features. For instance, the design of porous ceramics often faces trade-offs (porosity vs strength, pore structure vs strength, etc.) in engineering applications. When pursuing multiple and competing objectives, finding the most valuable solution that none of the target payoff can be improved without degrading the others, in game theory, is regarded as gradually approaching Nash equilibrium. In material design, the Nash equilibrium involves selecting such a subset of materials from the pool of all potential candidate materials in the design space, defined as those for which no additional enhancement of one objective (e.g. porosity) can be attained without compromising another objective (e.g. strength). And this subset can be referred to as the set of Pareto optimal materials (i.e. the Pareto front) [24-26]. The core goal of this work is focused on how to find a solution of this Nash equilibrium problem, taking the optimal design of freeze-cast porous Si_3N_4-Si_2N_2O ceramics as a model case. The establishment of this model is anticipated to facilitate the wider application of freeze-cast Si_3N_4-Si_2N_2O porous ceramics from high temperature to biomedicine.

For the microstructural and mechanical design of freeze-cast porous ceramics, it is vital to quantitatively understand and describe the process-structure-property relationship based on the analysis of hierarchical factors [27,28]. The mechanical properties of cellular materials in the Gibson-Ashby model are dependent on three factors: (i) the relative density of materials; (ii) the topology and shape of the cell edges and faces (i.e. pore structure); (iii) the properties of the solid of structure (i.e. composition and microstructure of walls) [29,30]. For the freeze-cast porous ceramics, as generally summarized in S. Deville's book [31], the detailed factors affecting their compressive strength are porosity (equivalent to relative density), solvent, pore size, microstructural gradient, orientation domains and connectivity, ice-lens like defects, and particle size.

As for freeze-cast porous ceramics from aqueous ceramic slurries, their porosity is mainly governed by solid loading and sintering parameter. Commonly, higher solids content and sintering conditions consistently lead to lower porosity and higher strength [32,33]. Considering specific needs, it may be essential to carefully balance the trade-off between porosity and strength sometimes. In the similar porosity case, the pore structure (primarily affected by the freezing front velocity (FFV)) would play a dominant role on the mechanical properties. To optimize the pore structure and hence improve mechanical properties, an appropriate FFV (always controlled by the cold finger's freezing temperature or cooling rate) is required. In general, there is a trend of increased compressive strength with faster FFV leading to smaller pore size and wall thickness according to the open online database (FreezeCasting.net) [34]. However, this rule is not universally applicable due to the joint interaction of multi-factors [35]. Moreover, the composition, initial particle shape and grain size of walls also have varying degrees of influence on the mechanical properties of materials [30,31,36-38]. Currently, the Gibson and Ashby micromechanical models for cellular materials are commonly utilized to describe the structure-property relationship. In the freeze-casting of the tert-butyl alcohol (TBA) system, the prediction of the out-of-plane honeycomb model successfully matches to the experimental values. However, the fitness is poor in the water-based system, due to the lamellar pore structure deviation from this model and the difficult-to-measure wall modulus [30,31,34,35,38].

The data science tools, particularly machine learning (ML), exhibit a powerful ability to reliably recreate experimental data and anticipate process-property correlation, and are widely employed in the design and prediction of alloys [39], ceramics [40], and concretes [41]. Multiple linear regression is a common

ML method for multivariate issues such as empirical equations between multi-level structural information and target property, and it has been effectively practiced in metals [42] and ceramics [43]. Although this method can mathematically convert some nonlinear relationships to linear relationships, the non-monotonic factors emerging in freeze-casting render it somewhat ineffective. The big data regression models of freeze-casting by K. L. Scotti and D. C. Dunand [34] are valuable for identifying outliers, roughly predicting the process-structure-property correlation, and comparing existing and freshly acquired data, but not general enough for tailoring materials to a specific application.

In the traditional application of ML for materials design, the microstructure is generally treated as a black box, and hence the optimal design process is implicit. As proposed by C. Suh *et al*. [44] in the outlook on ML, the understanding of material behaviors is equally important to the prediction of material properties. Microstructure information is the key to revealing materials' behaviors. A. Molkeri *et al*. [45] introduced a microstructure-aware Bayesian Optimization framework for goal-oriented materials design, proving that it is more effective and faster than the traditional microstructure-agnostic approach to solving problems.

Therefore, we establish a physics-based plus artificial neural network (ANN) hybrid data model of process-structure-property correlations (as illustrated in the workflow diagram in Figure 1), aiming to aid the mathematical understanding of the influence of hierarchical microstructural features (porosity, structural wavelength, composition and grain size) on the mechanical properties, and realize the microstructural and mechanical design of freeze-cast porous Si_3N_4-Si_2N_2O ceramics. And this proposed modeling path is expected to be extended to other freeze-cast porous ceramic systems to guide understanding and design.

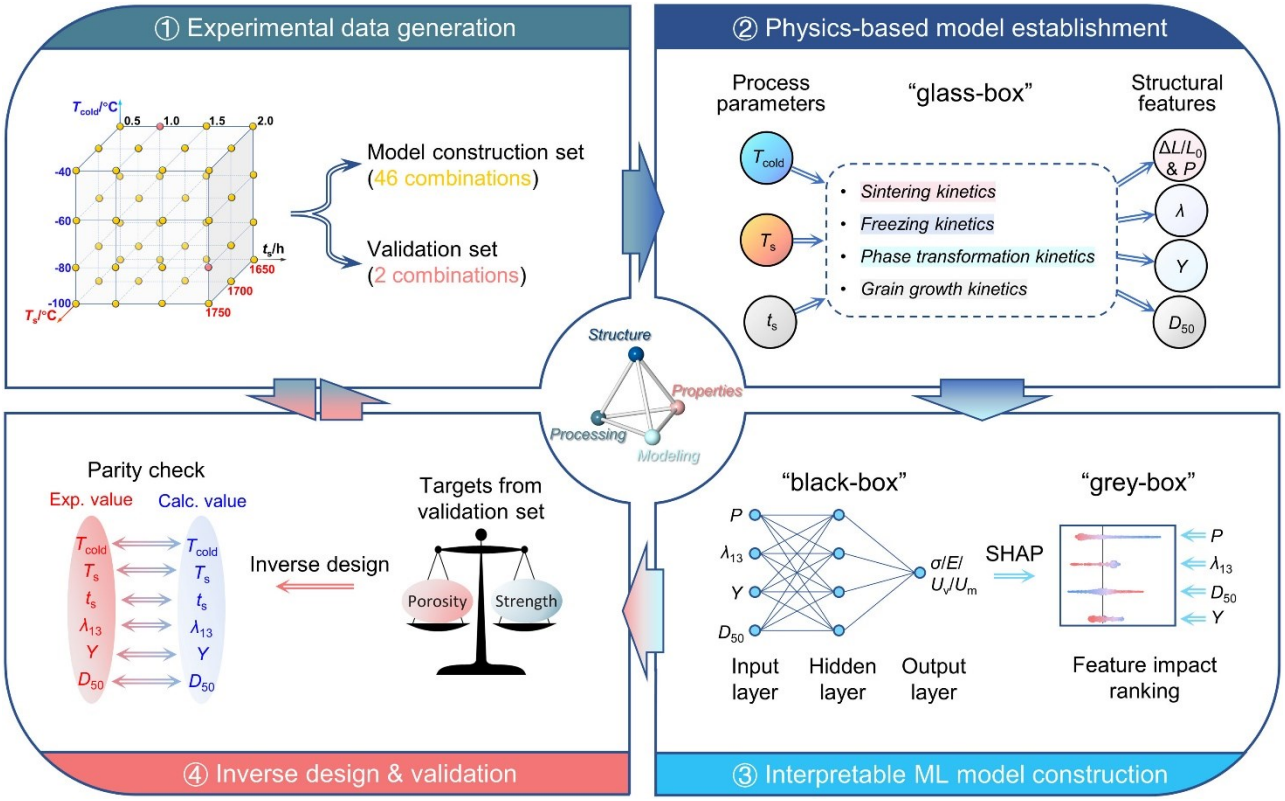

Figure 1 Workflow diagram of the physics-based/data-driven hybrid model, aiming at the structural and mechanical design of freeze-cast porous ceramics. This closed loop starts with the collection and division of microstructure (linear shrinkage rate of side length $\Delta L/L_0$, open porosity P, structural wavelength λ, phase content of β-Si_3N_4 Y, and median diameter of β-Si_3N_4 grains D_{50}) and property (compressive strength σ, stiffness E, energy absorption per unit volume U_v, and unit mass U_m) data over the entire process space (freezing temperature T_{cold}, sintering temperature T_s, and holding time t_s). Next, the kinetic relationship between process and microstructure, and further quantification of the correlation between microstructure and property are developed by an interpretable ANN model. Finally, the on-demand design capability of the hybrid model is evaluated by the two sets of validation data.

2. Materials and methods

2.1. Material preparation

Aqueous ceramic slurries were made using Si_3N_4 (α phase content>93 %, ~0.5 μm, Junyu Ceramic Plastic Products Co., LTD., Shanghai, P.R. China), fused SiO_2 (purity>99.5 %, ~0.6 μm, Guangyu Quartz Products Co., LTD., Lianyungang, P.R. China), Al_2O_3 (purity>98.0 %, ~0.75 μm, Showa Denko K.K., Tokyo, Japan) and Y_2O_3 (purity>99.0 %, ~2.9 μm, Yaoyi Alloy Material Co., LTD., Shanghai, P.R. China) with 20 vol.% solid loading. It should be noted that in this study, the primary focus is on the effect of sintering parameters on open porosity, while another nonnegligible factor, solid loading, is fixed at 20 vol.%. The molar ratio of Si_3N_4 and fused SiO_2 is 3:1, whereas that of Al_2O_3 and Y_2O_3 as sintering additives (total amount 10 wt.%) is 5:3. Tetramethylammonium hydroxide (TMAH, AR, 25 wt.% aqueous solution, Aladdin Biochemical Technology Co., LTD., Shanghai, P.R. China) and polyvinyl alcohol (PVA, DP ~1700, Macklin Biochemical Co., LTD., Shanghai, P.R. China) were added in the amounts of 0.4 wt.% and 2.0 wt.% (of the solids) as dispersant and binder, respectively. The homogeneous and stable slurries were simultaneously mixed and degassed in the TMV-1500T planetary centrifugal vacuum defoaming mixer (Smida intelligent equipment Co., LTD., Shenzhen, P.R. China) at 2000 rpm in a 35 kPa vacuum.

After stabilizing at room temperature, all the slurries in this investigation were directionally solidified with a custom-made freeze-casting system (details in Fig. S 1). The polytetrafluoroethylene (PTFE) mould filled with ~40 mL of the slurry was placed on the surface of a copper finger pre-chilled to the freezing temperature T_{cold} of −40 °C, −60 °C, −80 °C, −100 °C, while the top of the mould was left open to the atmosphere and kept at room temperature T_{hot} (~25 °C). The freezing front velocities for each freeze-casting condition were assessed using a "thermocouple" mould [30,46]. The "thermocouple" mould is designed with eight staggered thermocouples, spaced at 4 mm intervals along the height of the mould (see Figure 2(a) for details). To ensure the sensitivity of the in-suit temperature measurement and minimize the impact of thermocouples on the freezing process, seven thermocouples (~2 mm in diameter) were in direct contact with the slurry through the mould wall, without extending beyond it. Additionally, one extra thermocouple was positioned above the top of the slurry. The position of the freezing front was assumed to align with the 0 °C isotherm and evaluated by averaging three trials. Thus, the freezing front velocity was derived as the rate at which it travels along the height of the mould. Simultaneously, the local cooling rates were calculated for each thermocouple position. When fully frozen, the sample was demoulded with a punch and transferred to a pre-chilled freeze dryer (−50 °C and 1.5 Pa) to lyophilize for at least 48 h. Freeze-dried green bodies were gas pressure (0.5 MPa N_2) sintered at different sintering temperatures T_s (1650 °C, 1700 °C, 1750 °C) and holding times t_s (30 min, 60 min, 90 min, 120 min). The linear sintering shrinkage rate $\Delta L/L_0$ of the sample was calculated with the side length change before and after sintering. The open porosity P, apparent density ρ_a, and bulk density ρ_b of sintered samples were measured by Archimedes' buoyancy method. Specifically, open porosity P refers to the ratio of the total volume of the open pores in the scaffold to its bulk volume (include the volumes of the lamellar walls, all open pores and closed pores); apparent density ρ_a represents the ratio of the mass of the dry scaffold to its apparent volume (include the volumes of the lamellar walls and closed pores), which reflects the density of the lamellar walls; bulk density ρ_b refers to the ratio of the mass of the dry scaffold to its bulk volume, which indicates the density of the scaffold itself.

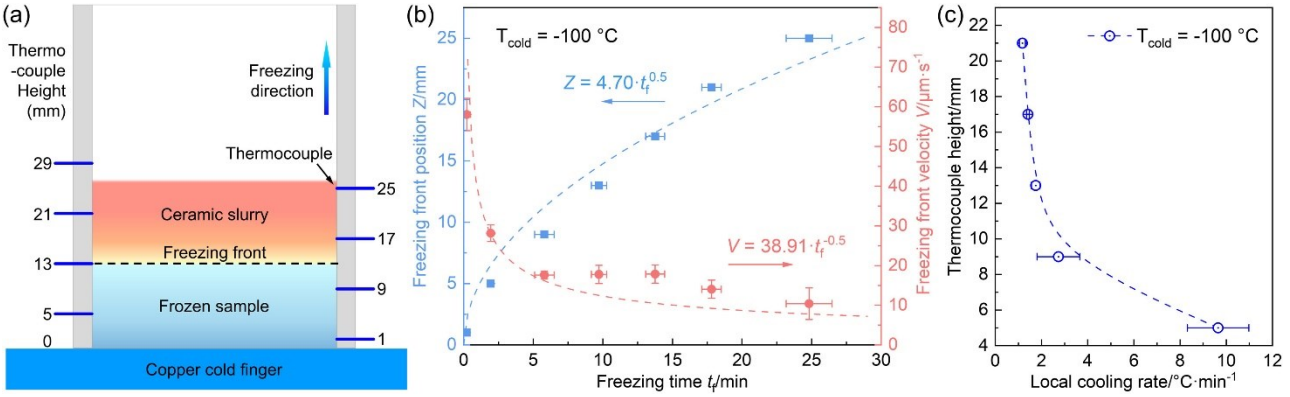

Figure 2 The "thermocouple" mould measurements along the freezing direction. (a) Schematic of the "thermocouple" mould. The measured and fitted position Z and velocity V of the FF (b), and the local cooling rates along the height (c) during freeze-casting at –100 °C.

2.2. Thermophysical properties of slurry and frozen solid for the two-phase Stefan problem

Based on several adequate hypotheses, the analytical solution to the two-phase Stefan problem under the Neumann condition was successfully applied to mathematically describe the steady-state freezing process [47,48]. Given that the two-phase Stefan problem is focused on the pure liquid, the thermophysical parameters of slurry and frozen solid were additionally adjusted and assumed to fulfill this model's premise in this study. First, densities of slurry (ρ_{slurry}) and frozen solid (ρ_{solid}), as well as the thermal conductivity of solid k_{solid}, were calculated using the volume fraction rule of mixtures. The thermal conductivity of slurry k_{slurry} was approximated by Jeffrey's model [49,50]. Next, the specific heat capacity of slurry (c_{slurry}) and frozen solid (c_{solid}) was estimated by the mass fraction rule of mixtures. Both the thermal diffusivity of slurry (α_{slurry}) and frozen solid (α_{solid}) can be given by

$$\alpha = \frac{k}{\rho c} \qquad (1)$$

Finally, on the basis of a reasonable assumption (only one heat release phase during freezing, i.e. water), the latent heat of fusion can be calculated by

$$L_{slurry} = \frac{(1-\emptyset)\rho_{H_2O}L}{\rho_{slurry}} \qquad (2)$$

where L_{slurry} and L are the latent heat of fusion for slurry and H_2O respectively, is the solid loading, and is the density of H_2O. The detailed thermophysical properties of pure water and slurry at room temperature (T_{hot}=25 °C) and minimum freezing temperature (T_{cold}=−100 °C) are available in the Supplementary Material.

2.3. Microstructural analysis: structural feature size, phase content and grain size of β-Si_3N_4

The structural feature size characterization of freeze-cast scaffolds was carried on the samples sintered at six typical sintering parameter combinations. As shown in Fig. S 3, each scaffold was first cut into rectangle parallelepipeds with a square basis of ~6 mm side length, and then the cubes were cut at 5 mm, 7 mm, 9 mm, 11 mm, or 13 mm from the bottom, respectively ("at X mm" in this study implies the height here). The structural feature size (containing pore size p, wall thickness w, and structural wavelength λ) of the freeze-cast porous ceramics was quantified by an upright super depth of field digital microscope (VHX-1000E, Keyence Corp., Osaka, Japan). At least three images per layer of the five 2 mm evenly spaced positions were captured at the same magnification. For each layer, over 50 pore size and wall thickness measurements were taken separately using the digital imaging software ImageJ [51] (ImageJ, U.S. National Institutes of Health, Bethesda, MD). And the structural wavelength of each layer was the sum of the mean pore size and the mean wall thickness obtained in that layer. Moreover, the pore size distribution (at ~13 mm) of the porous scaffold, prepared using several representative processes, was measured with a mercury intrusion porosimetry (Model Auto-pore IV 9500, Micromeritics, USA). The phase content of β-Si_3N_4 was quantitatively determined from X-Ray Diffraction

(XRD) data (using an Empyrean X-ray diffractometer, Malvern Panalytical LTD., Malvern, UK, with step size 0.013 deg, scan speed 1 °/min, and a large 2θ angular range of 10–130 deg) and subsequent Rietveld refinement carried on the open-source FullProf suite software. The sintered porous ceramics were crushed into fine powders in an agate mortar and sieved through a 325 mesh sieve (opening diameter ~44 μm) before XRD testing. After etching with hydrofluoric acid (AR, 40 %, Aladdin Biochemical Technology Co., LTD., Shanghai, P.R. China) for 5 min, the microstructure of sintered porous ceramics was observed on an SEM platform (Helios Nanolab 600i, Thermo Fisher Scientific Inc., Oregon, USA). Due to the occlusion of grains, the real length of the rod-like β-Si_3N_4 grains is hard to acquire. The median diameter (D_{50}) of β-Si_3N_4 grains was regarded as the grain size to describe their coarsening behavior in this study. D_{50} measurements were conducted using ImageJ from micrographs taken on over five different locations per specimen and at least 200 β-Si_3N_4 grains were measured for each sample.

2.4. Characterization of uniaxial compressive response at quasi-static regime and energy absorption

Small size samples (6 × 6 × 8 mm^3) were extracted from the section of each sintered scaffold between 5 mm and 13 mm away from the bottom for uniaxial compression testing. Compression experiments were carried out along the freezing direction at a low-strain rate (10^{-3} s^{-1}), corresponding to a cross-head speed of 0.5 mm/min, on an AGX-plus precision universal testing machine (Shimadzu Corp., Kyoto, Japan) with a 5 kN load cell. All samples fabricated by different processes (a total of 48 combinations of T_{cold}, T_s, t_s) were examined with 6~9 specimens per sample. To minimize lateral friction during uniaxial compressing, graphite sheets with a thickness of 40~50 μm were placed on the upper and bottom sides of the sample. Besides compressive fracture strength, post-fracture inelastic deformation and energy absorption characteristics of freeze-cast scaffolds are also critical factors affecting the mechanical reliability and performance of macro-porous components, especially under compressive loads [1,38,52]. The energy absorption ability of porous material can be evaluated by calculating the area under the compressive stress-strain curve. Thus, energy absorption capacity per unit volume (U_v) and unit mass (U_m) can be computed separately as:

$$U_V = \int_0^{\varepsilon} \sigma d\varepsilon \qquad (3)$$

$$U_m = \frac{U_V}{\rho_b} \qquad (4)$$

where ρ_b is the bulk density of porous ceramics. Here, the calculation of U_v and U_m were integrated to the 15 % strain (ε) value for each compressive stress-strain curve.

2.5. Machine learning (ML) architecture

Mathematically, an artificial neural network (ANN) model has been proved to be able to map any nonlinear object [53]. In the current work, a three-layer fully-connected feedforward ANN model was applied to construct the complex nonlinear relationships of process-structure-property (PSP). First, two groups of data with high porosity/low strength and low porosity/high strength were randomly isolated as the experimental validation for the generalization capability of the final PSP model. Then, the remaining 46 sets of data were randomly divided into training set and test set with a proportion of 85:15. The hyperparameters, including activation functions (rectified linear unit, hyperbolic tangent, and sigmoid), layer weights initial function (a uniform distribution with zero mean and variance of $2/N_I$ or $2/(N_I+N_O)$, here N_I and N_O are the input and output size of the layer), layer biases initial function (all with 0 or 1), and the number of neurons in the hidden layer (ranging from 4 to 10), were optimized by enumerating all possible combinations. During the optimization of hyperparameters, a 10-fold cross-validated model and L2-regularization with the strength of 0.02 were adopted to avoid overfitting. The ANN model was trained by minimizing the mean squared error (MSE) using the Limited-memory Broyden-Fletcher-Goldfarb-Shanno (LBFGS) algorithm [54]. After optimization, the best activation function was the hyperbolic tangent, and the layer weights initial function was a uniform distribution with zeros mean and variance of $2/(N_I+N_O)$. The best number of neural and layer biases initial functions were 4 and 0 for the PSP model, respectively. Finally, the model was reconstructed using the optimized hyperparameters. To get the corresponding process parameters and microstructural features of the target properties, the grid search with resolution of 1 °C in T_{cold} and T_s, and 1 min in t_s was applied to

explore the high-dimensional space. The SHapley Additive exPlanations (SHAP) [55] method was introduced to interpret this ANN model. The query points for SHAP were generated by uniform sampling 1000 points over the process parameters space.

3. Results

3.1. Analysis of freeze-casting temperature profiles within a "thermocouple" mould

The temperature profiles during freeze-casting under different T_{cold} conditions were recorded using a "thermocouple" mold equipped with eight evenly spaced thermocouples (as shown in Figure 2(a)). By reasonably assuming that the freezing front (FF) aligns with the 0 °C temperature contour [30,46,48,56], the position Z and velocity V of the FF, along with the corresponding regression fits, are depicted for four T_{cold} in Figure 2 (b) and Fig. S 2(a)-(c), respectively. As described in the Neumann solution ($Z \sim \sqrt{t_f}$ and $V \sim 1/\sqrt{t_f}$), where t_f is the freezing time) [57,58], when combined with the experimental V-t_f data, the freeze-casting process at a constant T_{cold} can be approximately divided into two stages: 1st stage, marked by a steep drop in FFV, and 2nd stage, exhibiting a more gradual decline in FFV. Specifically, in this study, it can be generally concluded that when the FF reaches the third thermocouple (i.e. Z = 9 mm), the freezing process enters the 2nd stage. As shown in Figure 2(b), the experimental FFV exhibits slight fluctuations between 17.6 ± 1.0 μm/s and 17.9 ± 2.3 μm/s during the freezing period from 5.8 ± 0.7 min to 13.8 ± 0.7 min (associated to the Z range of 9 mm - 17 mm). It can be approximated that the quasi steady-state has been reached within this range. This is also supported by the findings of S.M. Miller *et al*. [47,48]. The lamellar structures of interest at 13 mm are formed at exactly this stage.

In addition, the local cooling rate

at each thermocouple position decreases non-linearly with an increase in the thermocouple height. However, within the investigated range of freeze-casting conditions, the decline in the local cooling rate begins to slow down as the quasi steady-state directional solidification is achieved. Specifically, as depicted in Figure 2(c), taking T_{cold}=−100 °C as an example, the in the concerned range of 13 mm-17 mm, only gradually decreases from 1.75 ± 0.19 °C/min to 1.41 ± 0.06 °C/min. The corresponding local thermal gradient G=C/V [46] slightly reduces from 1.68 ± 0.42 °C/mm to 1.35 ± 0.25 °C/mm.

3.2. Sintering shrinkage rate, open porosity, and density

Linear sintering shrinkage rate, open porosity, and apparent density of samples prepared at the typical combinations of T_{cold}, T_s, and t_s are shown in Figure 3(a). As T_s and t_s increase, the linear shrinkage rate of porous ceramics rises steadily, while the porosity gradually falls. In the entire processing space, the linear shrinkage rate and porosity of the porous ceramics are in the range of 6.9 % ± 0.8 %~20.7 % ± 0.5 % and 60.7 % ± 1.2 %~77.4 % ± 1.7 %, respectively. It is worth mentioning that the influence of freezing temperature during freeze-casting on the shrinkage rate, porosity, and density is negligible in this case. In addition, the apparent densities of the sintered porous ceramics with different sintering parameters fluctuated between 2.9 g/cm^3 and 3.1 g/cm^3, suggesting that the sintering parameters have little effect on them, further indicating that there are nearly no closed pores in sintered scaffolds. Figure 3(b) shows the matrix scatter and correlation coefficient plot of the processing parameters, linear shrinkage rate, porosity, and bulk density for all samples. The absolute values of the Spearman correlation coefficients among the linear shrinkage rates, open porosities, and bulk densities are all very close to one, demonstrating a strong linear association among them. Thus, the linear quantitative correlations among those can be generated through the least-squares fitting. The linear fitting result of $\Delta L/L_0$ and P, for example, is as follows:

$$P = -0.9981\frac{\Delta L}{L_0} + 0.8476\,, \qquad R^2=0.9739 \qquad (5)$$

Furthermore, the comparison of the absolute value of the correlation coefficient also implies that the effect of holding time on sintering densification behavior of porous ceramics is slightly larger than that of sintering temperature. The correlation coefficients between freezing temperatures and shrinkage rates, porosities, densities, respectively, are nearly zero, confirming that freezing temperature has no significant effect on these factors.

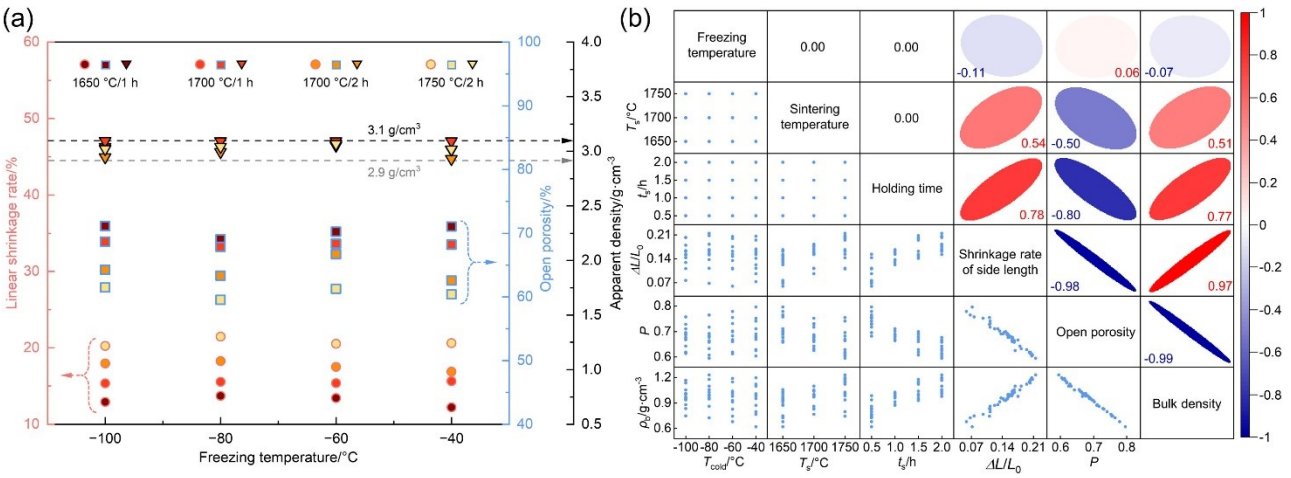

Figure 3 Correlation between process parameters and sintering behavior parameters. (a) Linear shrinkage rate of side length, open porosity, and apparent density of samples prepared by 16 typical processes. (b) The matrix scatter and correlation coefficient plot of all 48 samples, and the color bar indicates the Spearman correlation coefficient. Narrower colored ellipses in the upper right corner of the matrix plot represent stronger linear correlations and vice versa.

3.3. Microstructural analysis

As for the structural features of freeze-cast porous scaffolds, the pore size p, wall thickness w, and structural wavelength λ are mainly analyzed here. The height of feature size measurement from the bottom is indicated by the subscript number (e.g. p_9 means the pore size measured at 9 mm from the bottom). The statistical analysis of p and w distributions in Section 5-13 mm away from the bottom of sample shows that they both follow a normal distribution at a significance level of 0.05 (as shown in Figure 4(a-d) the Q-Q plots and Anderson-Darling test results of p and w statistics of four representative samples). We investigate the correlation between the distribution of structural feature size at five cross-sectional heights and sintering parameters in the four T_{cold} cases, taking the Jensen-Shannon divergence D_{JS} to measure the similarity of two distributions. D_{JS} = 0 indicates that the two distributions are the same, and D_{JS} gradually increases as the similarity decreases. The statistical box plots and Jensen-Shannon divergence of two groups of representative p and w distributions under the selected six sintering processes are given in Figure 4(e). Taking the p_9 distribution of samples frozen at −100 °C as an example, 15 pairwise comparisons and D_{JS} calculations are performed on the statistical results of porous ceramics sintered under six typical sintering processes. Over 94 % of all 600 sets of D_{JS} results are less than 0.1, which implies that, in the current statistical results, the p or w distributions at one cross-sectional height of the samples sintered under different T_s and t_s combinations are highly similar, despite a ~14 % difference between the maximum and minimum shrinkage rates. Moreover, the pore size distributions (at ~13 mm) of the freeze-cast scaffolds at −60 °C and −100 °C, prepared under various sintering conditions, are evaluated using mercury intrusion porosimetry. The results, as illustrated in Fig. S 4(b) and (c), provide additional confirmation that the sintering parameters exert minimal impact on the pore size p. The possible explanation is that the average standard deviation (~1.9 μm) of the statistical p and w distributions is comparable to the shrinkage size in each structural unit. And it is also associated with the anisotropic sintering shrinkage of each structural unit at the micro-scale, wherein the shrinkage rate of lamella unit along the short axis of pores cut perpendicular to the freezing direction is significantly lower than that along the long axis [59]. Consequently, these two factors may contribute to the insensitivity of pore size p, wall thickness w, and structural wavelength λ to sintering parameters. In addition, at the macro-scale, the height shrinkage rate of the sintered scaffolds ranges from 6.7 % ± 0.7 % to 23.2 % ± 0.8 %. Considering the maximum and minimum height shrinkage rates in this study, the microstructural feature sizes at 16.9 mm and 13.9 mm (i.e. at 13 mm of the sintered scaffolds) of the green body can be found in Fig. S 5. The statistical measurements reveal that under the applied freezing conditions here, the range of 13.9 mm-16.9 mm in the structural analysis of the green body corresponds to the quasi steady-state stage, where these feature sizes exhibit no statistically significant fluctuations. This also implies that the influence of local cooling rate on the feature sizes is negligible during this stage.

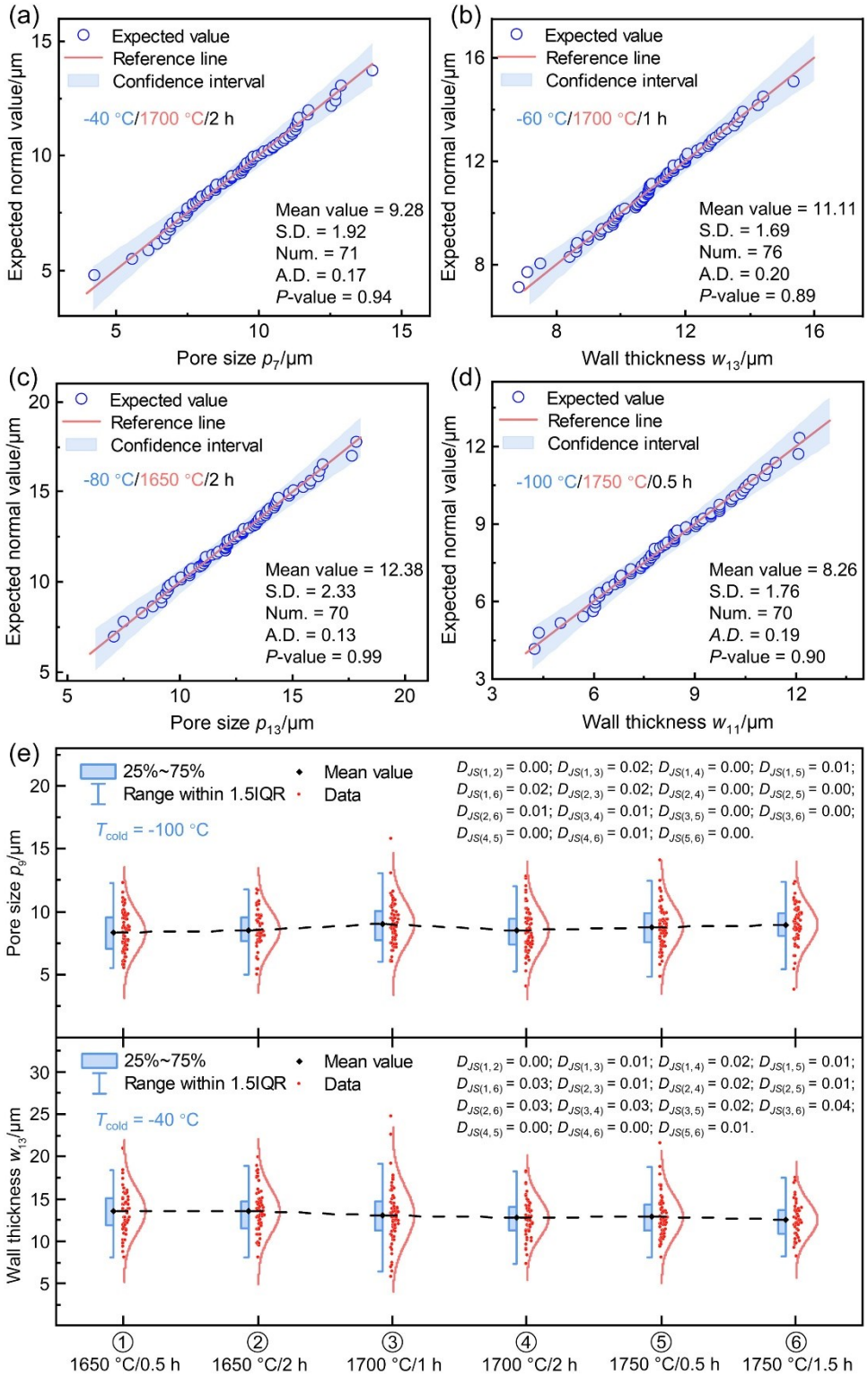

Figure 4 Statistical analysis of structural features (pore size p, wall thickness w, structural wavelength λ) of freeze-cast scaffolds. (a)-(d) Q-Q plots and Anderson-Darling test results of p and w statistics of four representative samples. Statistical parameters of distribution of structural feature size: S.D.–standard deviation, Num.–number of data, A.D.–test statistic for the Anderson-Darling test. (e) Box plots with data distributions of p and w for two frozen samples sintered at six parameter combinations. The subscript numbers (1, 2, 3, 4, 5, 6) of Jensen-Shannon divergence D_{JS} represent the serial numbers of the six sintering processes from left to right on the horizontal axis. For example, $D_{JS(1,2)}$ means the D_{JS} value of two p or w distributions of the samples sintered at 1650 °C/0.5 h and 1650 °C/2 h.

Figure 5(a) displays the average pore size p_{13}, wall thickness w_{13}, and structural wavelength λ_{13} at 13 mm of samples prepared under four freezing temperatures. When T_{cold} drops from −40 °C to −100 °C, λ_{13} also reduces from 29.4 ± 1.3 μm to 18.7 ± 0.2 μm due to the increase of ice crystal nucleation rate and freezing front velocity, and the declining trend of p_{13} is more noticeable than that of w_{13}. This is also consistent with the pore distributions obtained from mercury intrusion measurements of scaffolds frozen at different T_{cold} (refer to Fig. S 4(a)). The gradient of the feature size along the freezing direction

in two extreme situations (frozen at −40 °C and −100 °C) is illustrated in Figure 5(b). The lowest freezing temperature brings milder gradient of feature size. The quantitative relationship between structural wavelength and the height from the bottom are obtained through linear fitting, as listed in Table 1.

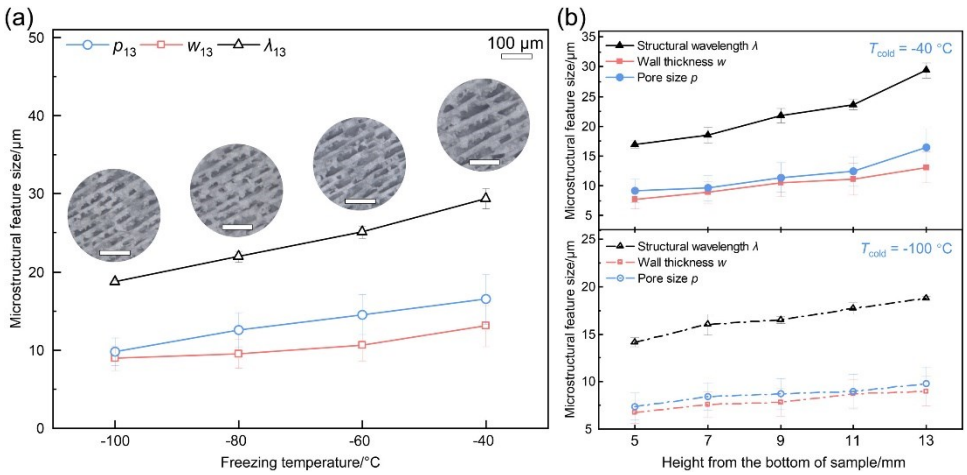

Figure 5 (a) Measured average microstructural feature size of freeze-cast scaffolds. (b) The gradient of feature size along the freezing direction in two extreme cases. The lines are only to guide the visualization and do not indicate expected values for intermediate feature size.

Table 1. Linear fitting results of the gradient of structural wavelength G_λ.

T_{cold}, °C	The gradient of structural wavelength G_λ, μm/mm	Intercept	R^2
−40	1.4991	8.5735	0.9481
−60	1.2284	8.5823	0.9881
−80	0.8060	11.7920	0.9994
−100	0.5468	11.7060	0.9739

Further, there is a significant linear correlation between λ_{13} and the gradient of structural wavelength G_λ, and the least-squares fitness can be found below:

$$G_\lambda = 0.0927\lambda_{13} - 1.1853 \qquad R^2=0.9787 \qquad (6)$$

The phases evolution of the −100 °C freeze-cast samples with various sintering parameters is quantitatively characterized by X-ray diffraction coupled to Rietveld refinement (two quintessential XRD refined fitting results are shown in Fig. S 6). The increase of T_s and t_s promotes the phase transformation of α-Si_3N_4 to β-Si_3N_4. The content of each phase in samples sintered at 1650–1750 °C for 0.5–2 h is marked in Figure 6. The Si_2N_2O phase is being used in this study to further improve the oxidation resistance and dielectric properties of porous Si_3N_4 ceramics. The wt. fraction of Si_2N_2O only varies between 31.5 % and 34.8 % except for that of the sample sintered at 1750 °C/2 h. This not only indicates that the reaction between fused SiO_2 and Si_3N_4 has been finished before 1650 °C but also suggests that a prolonged holding time at high temperatures under nitrogen may cause a minor decomposition of Si_2N_2O.

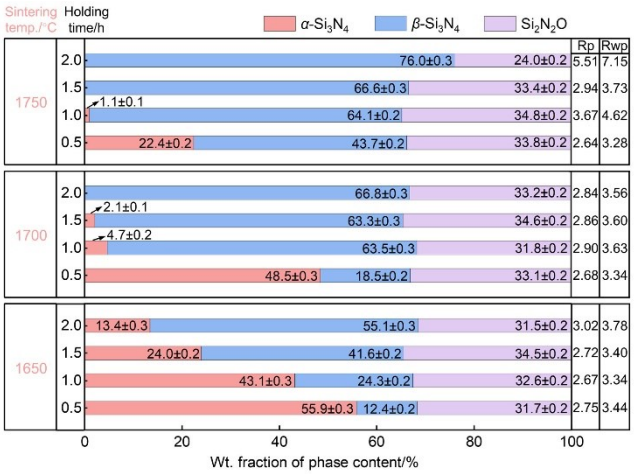

Figure 6. The wt. fraction of each phase calculated by Rietveld refinements for the samples fabricated at all sintering cycles.

Figure 7 shows SEM micrographs of grains in porous ceramics sintered at 1650–1750 °C for 0.5–2 h. Due to the enhancement of mechanical properties by well-grown rod-like grains [21,60], the coarsening behavior of the scaffold microstructure in this work concentrates on β-Si_3N_4. The quantity and grain size of β-Si_3N_4 are rising "with the naked eye" as the sintering time and temperature increase, and α-Si_3N_4→β-Si_3N_4 phase transformation develops, with D_{50} ranging from 142 to 464 nm.

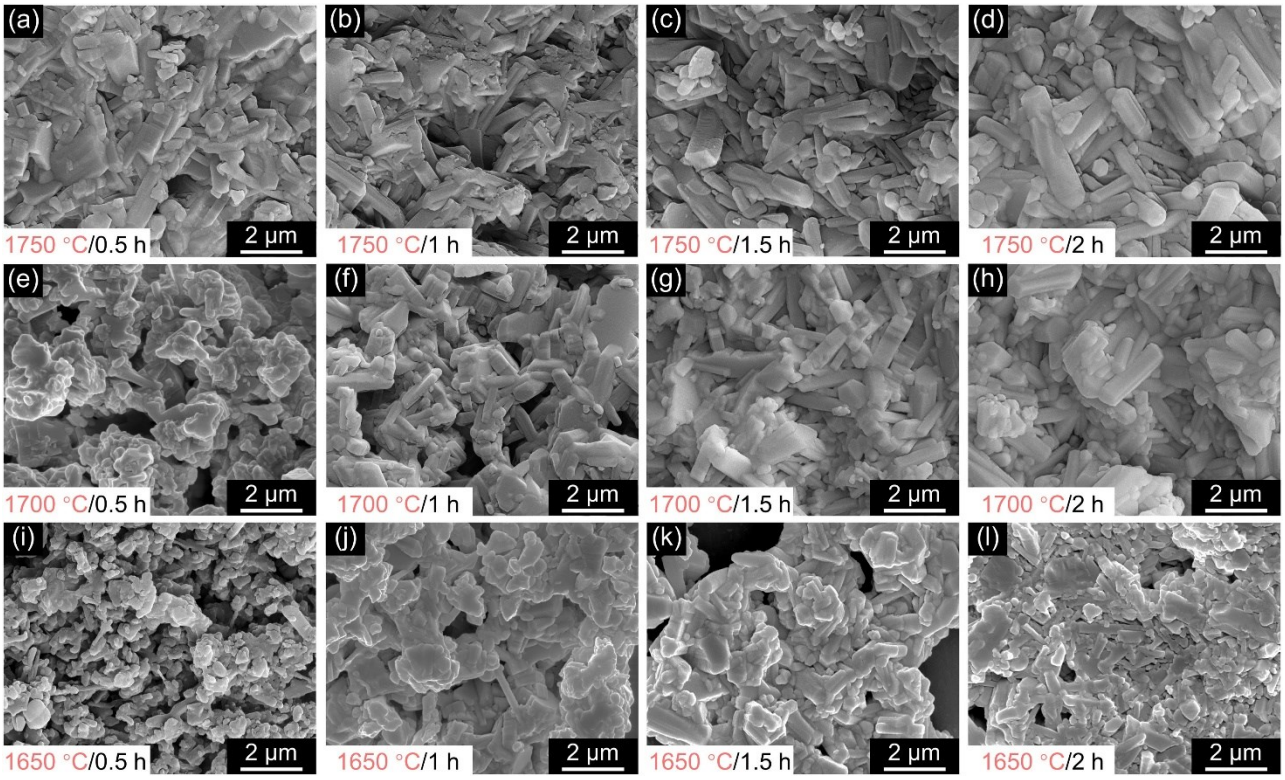

Figure 7 SEM micrographs of the grain morphology of porous Si_3N_4-Si_2N_2O ceramics sintered at 1650–1750 °C for 0.5–2 h.

3.4. Quasi-static uniaxial compressive response and energy absorption

Within a wide range of compressive strength (5.4 ± 1.1–44.1 ± 5.5 MPa) and stiffness (0.20 ± 0.03–1.81 ± 0.23 GPa), all sintered scaffolds' quasi-static (strain rate ~10^{-3} s^{-1}) uniaxial compressive responses exhibit a graceful progressive failure. Specifically, all the stress-strain curves are observed to be nearly similar mechanical responses, that is, a linear rise of stress with strain and subsequent pseudoplastic descent of stress with further strain increments.

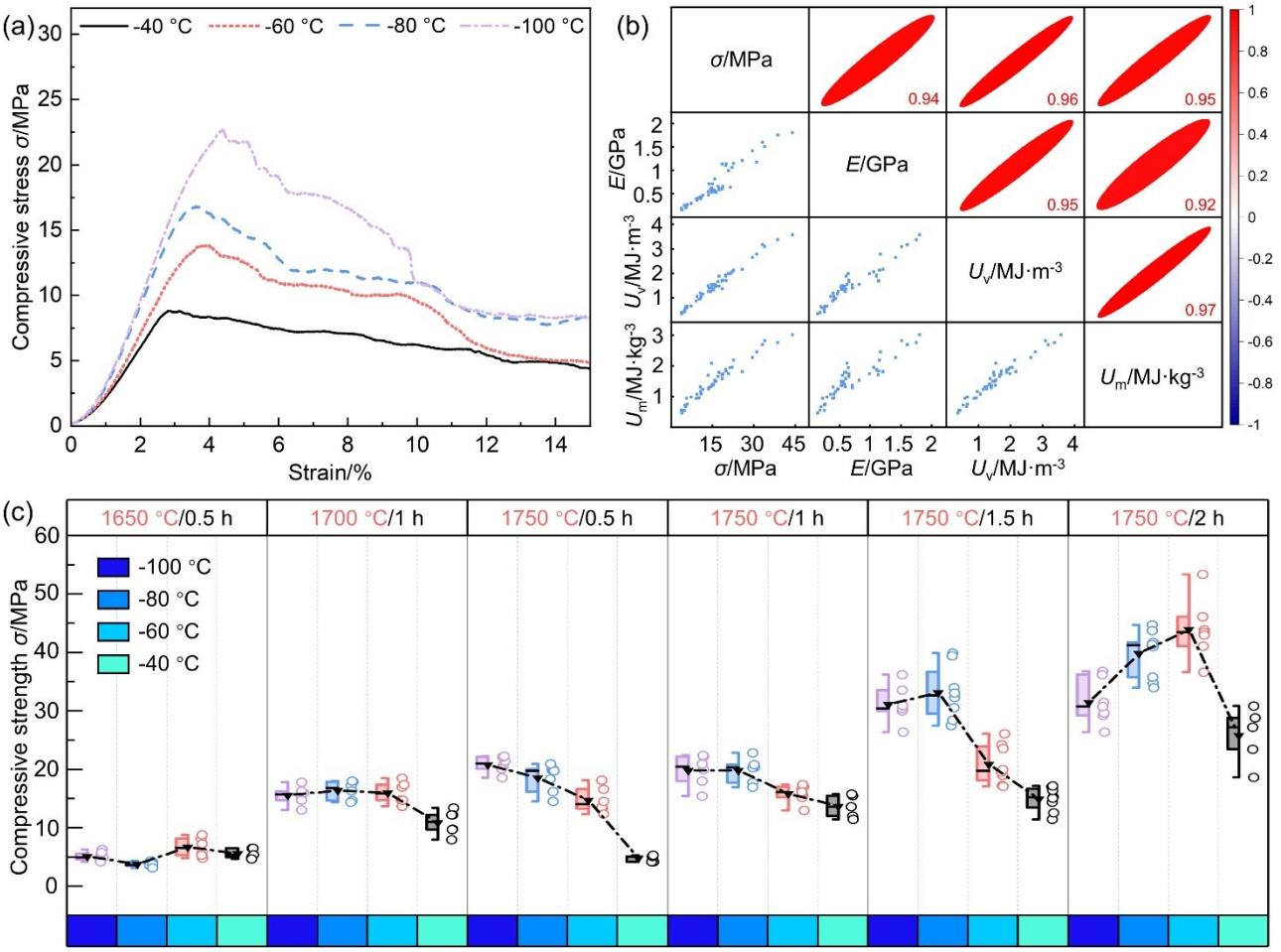

Figure 8 Quasi-static uniaxial compressive response of freeze-cast scaffolds. (a) Example compressive stress-strain curves up to 15 % strain for specimens frozen at −40 °C to −100 °C (sintered at 1700 °C/ 1.5 h). (b) The matrix scatter and correlation coefficient plot of all observed mechanical properties (compressive strength σ, stiffness E, energy absorption per unit volume U_v, and unit mass U_m), and the color bar indicates the Spearman correlation coefficient. (c) Comparison of compressive strength of samples manufactured with different process parameters (each color block represents a distinct freezing temperature, while the upper parameters correspond the combined values of sintering temperature and holding time).

Figure 8(a) shows example compressive stress-strain curves up to 15 % strain for specimens frozen at −40 °C to −100 °C (sintered at 1700 °C/ 1.5 h). In addition, the correlation analysis of the observed compressive strength, stiffness, energy absorption per unit volume, and unit mass (as shown in Figure 8(b)) reveals a strong and positive linear correlation among them, with the Spearman correlation coefficients of 0.92–0.97. Mostly, the compressive strength improves when the freezing temperature drops, as seen in Figure 8(a). This is not the full story and its evolution with freezing temperature changes depending on sintering settings. As illustrated in Figure 8(c), there is a general trend that the samples with the highest mechanical properties will be those frozen between −60 °C and −80 °C when the sintering parameters raise. With decrease of freezing temperature, the reduced defect (i.e. pore) size, the uniform distribution of load across lamellar walls, and the increased number of bridges between parallel walls that preventing their Euler buckling would contribute to the enhancement of mechanical properties [30,32,35,61-63]. In addition, the smaller and narrower distribution of the wall thickness would result in a higher Weibull modulus of materials [64]. However, the smaller wall thickness caused by a higher FFV unavoidably decrease the critical Euler buckling stress and consequently reduces the strength. For example, the compressive strength and stiffness of porous yttria-stabilized zirconia (YSZ) ceramics with high porosity would drop by 7 % to 37 % when the cooling rate exceeds 10 °C/min and approaches to 40 °C/min [65]. The optimized T_{cold} range for the higher strength is probably caused by a trade-off between the connection density and the critical Euler buckling stress of freeze-cast scaffolds.

3.5. Correlation analysis of sintering shrinkage behavior and sintering process

To quantify the liquid-phase sintering behavior in the Si_3N_4-SiO_2-Al_2O_3-Y_2O_3 system, Kingery's model [66-68] can be used to establish the mathematical relationship between linear shrinkage rate and sintering parameters as follows (Eq.(7)):

$$\frac{\Delta L}{L_0} = k_s \times t_s^{n_s} \qquad (7)$$

Where $\Delta L/L_0$ is the linear shrinkage rate measured after the sintering process at absolute temperature T_s for a duration t_s, k_s is the kinetic constant ($k_s = k_{0s}\cdot\exp(-Q_s/RT_s)$), R is the gas constant, Q_s is an apparent activation energy for sintering, and k_{0s}, n_s are constants.

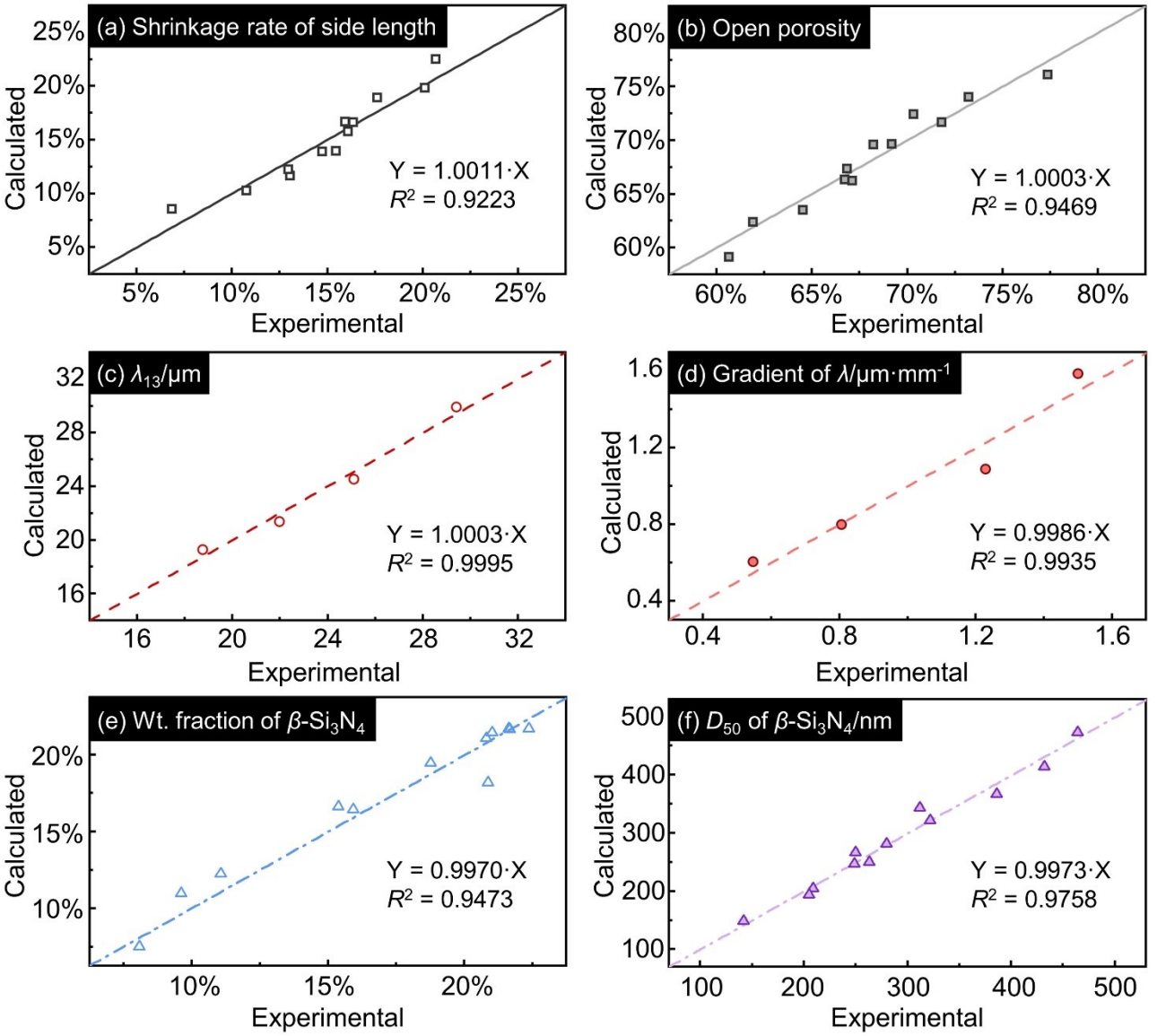

Figure 9 Parity plots of the calculated and experimental values of (a) ΔL/L₀, (b) P, (c) λ₁₃, (d) Gλ, (e) Y, (f) D₅₀. Both the slopes of the regression lines and the R² values, close to 1, exhibit a well-fitting prediction ability.

As stated in previous results of R. E. Loehman *et al.* [69], and D. Suttor *et al.* [70], the apparent exponent n_s (shown in Table 2) fitted in this work are also slightly larger than that expected by Kingery's model (n_s=0.33 or 0.20), suggesting that a variety of sintering mechanisms, including solution-precipitation and $\alpha \rightarrow \beta$ phase transformation and so on, are probably active during the intermediate stage for Si_3N_4-SiO_2-Al_2O_3-Y_2O_3 system. Furthermore, the apparent activation energy (115.2 kJ/mol) in this study is lower than that reported by O. Abe (193.1 kJ/mol [71]) and G. R. Terwilliger *et al.* (164.1 kJ/mol [72]), showing that the chemical reaction of Si_3N_4 and fused SiO_2, as well as the increment of the actual liquid phase to 19.47 wt.% ± 0.75 wt.% in all samples due to incompletely reacted SiO_2, promote the diffusion of N atoms during sintering and bring out a smaller Q_s in this system. Furthermore, the composition of

the liquid phase in this study differs from that in previous cases, which constitutes one of the key factors contributing to the disparity in activation energy. Combined with the prior linear fitting between shrinkage rate and open porosity, their calculated values closely match the experimental values, as shown in Figure 9(a) and (b), respectively.

Table 2. Summary of the parameters of microstructural kinetic models (Eq. (7), Eq. (13) to (16)).

$\Delta L/L_0$, %	k_{0s}	Q_s, kJ/mol	n_s
	25.72	115.2	0.44
λ, μm	φ	m	n_f
	0.30	75.9	0.50
Y, %	k_{0Y}	Q_Y, kJ/mol	n_Y
	$6.62\cdot10^{13}$	637.1	1.82
D_{50}, nm	k_{0G}, nm^2/s	Q_G, kJ/mol	n_G
	$2.44\cdot10^{11}$	365.0	2.18

3.6. Correlation analysis of structural wavelength and freezing temperature

The structural characteristics and properties of lamellar structure in the steady-state region are more frequently concerned for freeze-cast scaffolds, while the parts of the initial and transition region (generally thinner than 2 mm) are often excised [73,74]. It is necessary to establish the quantitative relationship between λ and T_{cold} from the theory of solidification.

Firstly, the Neumann solution to the two-phase Stefan problem provides the equations for the position Z and velocity V of the freezing front during solidification, given by

$$Z(t_f) = 2\Lambda\sqrt{\alpha_s t_f} \quad (8)$$

$$V(t_f) = \Lambda\sqrt{\alpha_s / t_f} \quad (9)$$

where Λ is solved by the following transcendental equation

$$\Lambda\sqrt{\pi} = St_s/exp(\Lambda^2)erf(\Lambda) - St_1/\mu v exp(\mu^2 v^2 \Lambda^2)erf(\mu v \Lambda) \quad (10)$$

with the Stefan number of frozen solid $St_s = c_{solid}(T_m\text{-}T_{cold})/L_{slurry}$, the Stefan number of slurry $St_l = c_{slurry}(T_{hot}\text{-}T_m)/L_{slurry}$, the melting temperature of slurry (T_m=0 °C), $\mu = \rho_{solid}/\rho_{slurry}$, $v = \sqrt{\alpha_{solid}/\alpha_{slurry}}$. Simply, the coefficient term ($k_f = 2\Lambda\sqrt{\alpha_s}$) of Eq. (8) can be fitted from the in-situ temperature profiles measured using the "thermocouple" mould (refer to Figure 2(b) and Fig. S 2(a)-(c)). However, when compared to the predicted coefficient based on the thermophysical characteristics of slurry and the freezing temperature, the calculated value k_f is only ~30 % of the predicted. This suggests that in fact, the absence of a perfectly adiabatic sidewall to generate a single vertical heat flow causes the observed freezing front kinetics to be slower than predicted by the Stefan problem model, as reported by S. M. Miller *et al*. [47,48]. Thus, a pre-factor φ is added to deal with the gap between the excepted and actual kinetics. This empirical pre-factor is calculated by

$$\varphi = \frac{k_f}{\Lambda} \quad (11)$$

The pre-factor falls just a little from 0.31 to 0.29 as T_{cold} drops from −40 °C to −100 °C, hence the average of them (~0.30) is taken to adapt this model. And the corrected Eq. (8) and Eq. (9) from experimental data are presented below:

$$Z(t_f) = 2\varphi\Lambda\sqrt{\alpha_s t_f} \quad (12)$$

$$V(t_f) = \varphi\Lambda\sqrt{\alpha_s / t_f} \quad (13)$$

Secondly, based on the analysis of the in-situ temperature profiles and the structure of green body, it can be found that: 1) the quasi steady-state directional solidification can be approximately achieved

within the range of 9 mm - 17 mm; 2) the slight decrease in the local cooling rate between 13.9 mm and 16.9 mm have a negligible impact on the lamella structure under the freezing conditions of this study. Hence, the well-demonstrated empirical power-law dependency of λ on freezing front velocity in the freeze-casting field could be applied [31,34,47,48]:

$$\lambda = m \times V^{-n_f} \qquad (14)$$

where m is a constant and the exponent n_f typically varies from 0.03 to 1.3 [34]. Here, the concerned structural wavelength at 13 mm of the sintered scaffolds is quantified. And a common exponent n_f of 0.50 is derived by the regression fitting of λ_{13} and V_{13}.
Lastly, the predicted gradient value along the freezing direction could be further calculated using the linear regression of λ_{13} and G_λ (i.e. Eq. (6)). The parity plots (as presented in Figure 9(c) and (d)) of the predicted and observed λ_{13} and G_λ of the samples prepared at four freezing temperatures present a good fitness of this model.

3.7. Correlation analysis of microstructure and sintering parameters

In the Si_3N_4-Si_2N_2O system, more well-developed rod-like β-Si_3N_4 grains play a vital role in the strength of sintered scaffolds. Therefore, the kinetics between the microstructure of β-Si_3N_4 (phase content and grain size) and the sintering parameters are determined in this work.
The $\alpha \rightarrow \beta$ phase change of Si_3N_4 belongs to a classic nucleation-growth type first-order phase transition. This heterogeneous phase transition can be described by the Johnson-Mehl-Avrami equation [75,76]:

$$Y = 1 - exp\left(-k_Y \times t_s^{n_Y}\right) \qquad (15)$$

where Y is β-Si_3N_4 wt. fraction transformed after sintering at absolute temperature T_s for a holding time t_s, k_Y is the kinetic constant ($k_Y = k_{0Y} \cdot \exp(-Q_Y/RT_s)$), R is the gas constant, Q_Y is an apparent activation energy for phase transition, and k_{0Y} and n_Y are constants. The Avrami exponent n_Y, which varies depending on the transformation mechanism, is usually between 1 and 4 [77]. For Si_3N_4 based system, the n_Y value also changes with the liquid quantity and composition. The fitted exponent n_Y (shown inTable 2) in this work is higher than those reported by J. C. Almeida *et al*. (0.67–0.90 [78]), A. Bandyopadhyay *et al*. (0.14–1.13 [79]), and S. Ordoñez *et al*. (0.6–1.3 [80]), indicating that the Si_3N_4-SiO_2 reaction and the increase of the actual liquid phase content during sintering make the phase transition faster than theirs. And the activation energy Q_Y also varies greatly relying on the liquid phase, ranging from 340 to 770 kJ/mol [81-84]. In this case, the regression-analysis Q_Y value is 637.1 kJ/mol.
The β-Si_3N_4 grain growth is generally recognized to be the anisotropic Oswald ripening regulated by the solution-reprecipitation mechanism [85-87]. Although previous research pointed that there exist some mismatches with the assumptions of the Lifshitz-Slyozov-Wagner (LSW) theory in the Si_3N_4 system [88,89], this theory still achieves good fits in the attempts of K. R. Lai and T. Y. Tien [90], H. Bjorklund *et al*. [91] and G. Bernard-Granger *et al*. [92]. Thus, the coarsening kinetics of β-Si_3N_4 can be characterized by the following empirical equation:

$$D_{50}^{n_G} = k_G \times t_s \qquad (16)$$

where D_{50} is the median diameter of β-Si_3N_4 grains after sintering at absolute temperature T_s for a holding time t_s, k_G is the growth rate constant ($k_G = k_{0G} \cdot \exp(-Q_G/RT_s)$), R is the gas constant, Q_G is the apparent activation energy of coarsening, and k_{0G} and n_G are constants.
Differing from the growth exponent (n_G= 2 or 3 depending on the coarsening mechanisms) predicted in LSW theory, the formerly fitted n_G values are 3~5 in diameter direction[90-92]. But the calculated n_G, in this case 2.18, is lower than previously reported, implying that the growth in diameter would be faster, which may be caused by the Si_3N_4-SiO_2 reaction and inhibitory effect of Si_2N_2O (28.2 vol.% ± 2.71 vol.%) on β-Si_3N_4 grain growth in length direction during sintering. In addition, the apparent activation energy of coarsening is also directly linked to the composition, with a Q_G of 365.0 kJ/mol found here. Figure 9(e) and (f) display the comparison of the calculated and experimental values of Y and D_{50}, respectively, which suggests a satisfying prediction ability of the phase transition and coarsening kinetic model.
3.8. Prediction of mechanical properties from the process and microstructural parameters

In this work, the process-structure-property (PSP) model via physics-based plus ANN hybrid methods is employed to quantitatively predict the mechanical properties of freeze-cast porous Si_3N_4-Si_2N_2O ceramics. Besides the evident factors of open porosity and structural wavelength, it is crucial to recognize the significance of phase composition and grain size in the freeze-cast scaffolds [30,37,38,93], which are also incorporated into the PSP model.

Firstly, four kinetic equations (for sintering, freezing, phase transformation, and coarsening) are applied to bridge process and structure, and then four hierarchical microstructural parameters (open porosity P, structural wavelength λ_{13}, β-Si_3N_4 wt. fraction Y and median diameter D_{50}) are input into the ANN model as a set of feature descriptors. The outputs are mechanical properties including compressive strength σ, stiffness E, energy absorption per unit volume U_v, and unit mass U_m. Because of strong positive correlations among the four mechanical properties and their similar evolution with the processes and microstructural parameters, the prediction and analysis of the compressive strength are mainly discussed here. In addition, we train a traditional process-property (PP) black-box model together for comparison, also see the Supplementary Materials for details.

Taking correlation coefficient (R) and root mean squared error (RMSE) as the evaluation metrics for the model construction, the PSP model exhibits the same level of accuracy as the traditional PP model. Figure 10(a) and (b) depict the predicted and observed compressive strength in the training set and test set from the PSP model, respectively. With regard to the training set, it is evident that nearly all data points and their least-squares fit line (displayed as the purple solid line) are located around the diagonal (as shown by the black dashed line), while the R and RMSE of the PSP model is 0.96 and 2.5, respectively, implying that the predictions are in good agreement with the experimental results. As for the test set, the R of the PSP model equals to 0.92, indicating the generalization ability of this model to some degree. Additionally, the compressive strength heatmap in Figure 10(c) predicted by the PSP model draws a similar trend consistent with the experimental results, that is, the freezing temperature for optimizing the compressive strength gradually changes from −100 °C to approximately −60 °C with the increase of the sintering parameters, and the corresponding predicted σ_{max} reach 39.4 MPa (experimental σ_{max} 44.1 ± 5.5 MPa under the corresponding process).

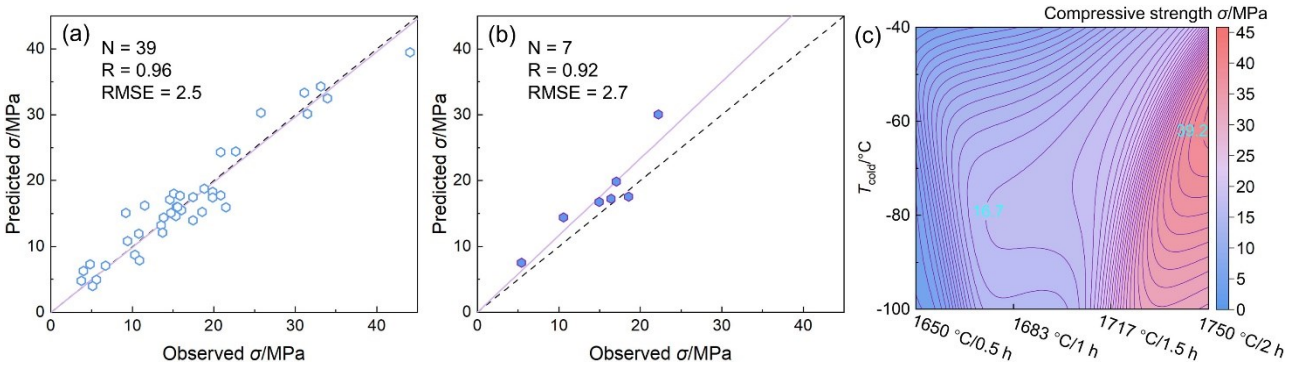

Figure 10 The predicted compressive strength σ as a function of the observed σ for (a) the training set and (b) the test set of the PSP model, respectively. N represents the number of data. (c) Compressive strength heatmap predicted from the PSP model. The x-axis of the heatmaps physically represents the combination of sintering parameters that fall on the diagonal line of sintering temperature and holding time.

4. Discussion

4.1. SHAP analysis of the PSP model

In the PSP route, although the explicit kinetic models are glass-box models, the lack of interpretability of the structure-property ANN model still hinders our further microstructural insights and understanding of materials design rules.

The SHapley Additive exPlanations (SHAP) [55,94-97], as one indispensable branch of the interpretable machine learning models, shines a light on quantifying the relative impact of descriptors on target outputs. On the one hand, a feature descriptor's SHAP value represents its average marginal contribution, and positive SHAP values are associated with model predictions of high target outputs and vice versa. Wider horizontal coverage of SHAP value for one feature descriptor, on the other hand, means a greater impact on the target outputs of one ML model. The global SHAP value (i.e. the average of the absolute SHAP values of each feature descriptors) is further employed to quantitatively rank their importance to the model predictions.

As demonstrated in Figure 11(a), the feature importance calculated by SHAP analysis for the PSP model elucidates that the porosity P among the four microstructural parameters plays the most influential role in the compressive strength. For cellular solids or porous materials, whether from the Ryshkewitch empirical equation [98-100] or the Gibson-Ashby model [1,29], porosity or relative density is the most critical factor determining their mechanical properties. In the next hierarchical level, the second-ranked λ_{13} with a global SHAP value of 2.421 also has a non-negligible effect on the mechanical properties. The development of the subsequent D_{50} and Y at a more microscopic hierarchical level is conductive to strengthen porous ceramics.

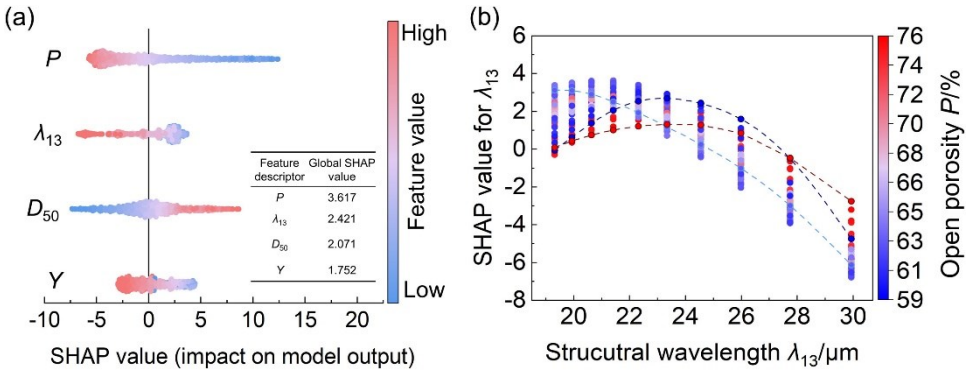

Figure 11 The SHAP analysis of the ANN model. (a) The feature descriptors' importance ranking of the PSP model (including open porosity P*, structural wavelength* λ_{13}*, median diameter of* β-Si_3N_4 *grains* D_{50}*, and phase content of* β-Si_3N_4 *Y). (b) The scatter plot of SHAP value for structural wavelength* λ_{13}*. The y-axis SHAP values evaluate the contribution of individual features to compressive strength calculated from the models. The color bar is mapped to a second feature value, to highlight the feature interaction.*

Furthermore, Figure 11(b) provides the SHAP values for λ_{13}, as a function of λ_{13}. And the vertical spread in SHAP values displays the feature interaction effect with open porosity P (indicated in the color bar). As for the effects of open porosity and structural wavelength on the compressive strength, the fluctuation of the SHAP value for λ_{13} should be explored in the following sub-cases. In Figure 11(b), three representative curves of the SHAP value as a function of λ_{13} are retrieved when P is 76.1 %, 64.9 %, and 59.1 % (corresponding to the dark red, light blue and dark blue dashed lines, respectively). For the high porosity case (nearly 73.5 % ~ 76.1 %), e.g. P = 76.1 %, the SHAP value barely ranges between −2.758 and 1.313, indicating that the structural wavelength exerts a weak influence on the compressive strength. In the medium porosity range (about 63.9 % ~ 73.5 %), the typical SHAP value declines gradually from 3.131 to −6.124 (marked by the light blue dashed line) as λ_{13} increases from 19.3 μm to 29.9 μm, suggesting that the structural wavelength has a remarkable negative correlation with the compressive strength. When the porosity is further lowered to the range of 59.1 % ~ 63.9 %, the approximate parabolic relationship between the SHAP value and λ_{13} (illustrated by the dark blue dashed line) implies that an optimal structural wavelength exists to maximize compressive strength. Previous studies have proven that the freezing condition or structural wavelength has multiple possible effects on the mechanical properties of freeze-cast porous ceramics [35]. The influences of structural wavelength change over three porosity ranges in this work, which may result from the trade-off between separate factors (including connection density and critical buckling, etc.). The quantitative analysis of the effect of microstructures on strength will assist the structural and mechanical design of freeze-cast porous ceramics in practice.

4.2. Experimental validation of the inverse design ability of the PSP model

For engineering applications, e.g. tissue engineering scaffolds, the design of porous ceramics often faces trade-offs including porosity vs strength, pore structure vs strength, etc. Two sets of extreme-case experimental data (target of case #1 and #2: P 71.0 % ± 0.5 %/σ 6.3 ± 0.4 MPa and P 59.5 % ± 1.3 %/σ 39.8 ± 4.0 MPa, respectively) isolated before the model construction are employed to verify the structural and mechanical inverse design ability of the PSP model.

Two groups of the process parameters and other feature descriptors from the inverse design of the PSP model are listed in the Table 3. In these two cases, except that the relative error (RE) of β-Si_3N_4 wt. fraction Y in case #1 reach 13.6 %, the prediction error of the process and microstructure parameters are all within 10 %, showing a robust and reliable inverse design potential for diverse demands. It can be noted from the phase transformation kinetics that the RE of Y results from the sensitivity of the sintering parameters at the early and middle stage, implying that a small variation in the sintering

parameters would cause a visible change in the β-Si_3N_4 wt. fraction. This prediction error can be reduced rapidly after fine-tuning the process in future reverse engineering.

Table 3. Comparison of the experimental validation of the PSP model.

Case No.		Targets		Process parameters			Other feature descriptors		
		P, %	σ, MPa	T_{cold}, °C	T_s, °C	t_s, h	Y, wt.%	λ_{13}, μm	D_{50}, nm
#1	Exp. value	71.0 ± 0.5	6.3 ± 0.4	−40	1650	1	24.3 ± 0.2	29.4 ± 1.3	209
	Calc. value	72.6	6.6	−40	1650	0.97	27.6	29.9	201
	RE	+2.3 %	+4.8 %	0	0	−3.0 %	+13.6 %	+1.7 %	−3.8 %
#2	Exp. value	59.5 ± 1.3	39.8 ± 4.0	−80	1750	2	76.0 ± 0.3	22.0 ± 0.7	464
	Calc. value	59.7	37.7	−76	1750	1.9	73.2	21.9	462
	RE	0.3 %	−5.3 %	5.0 %	0	−5.0 %	−3.7 %	−0.5 %	−0.4 %

Taking the porosity P vs strength σ trade-off in tissue engineering scaffolds as an example, the trade-off plot of performance metrics $P_1 = 1/P$ and $P_2 = 1/\sigma$ for this application is shown in Figure 12. In addition, Figure 12 also gives the Pareto front (red dotted line) predicted by the PSP model for this pair of competitive goals (where star marks represent the corresponding measured data points). For the cancellous bone (usually porosity of 50 %~90 %) tissue scaffolds, freeze-cast Si_3N_4-Si_2N_2O ceramics in this work show most of advantages over common freeze-cast material systems such as the hydroxyapatite (HAP) within a porosity range of 59 %~76 %. On this basis, the optimized inverse design of the materials with target porosity and strength can be achieved in this range.

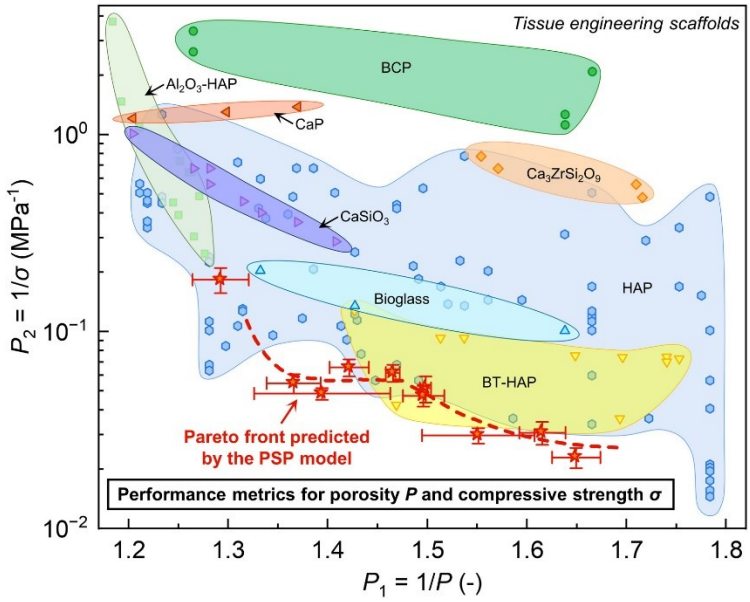

Figure 12 The trade-off plot of performance metrics $P_1 = 1/P$ and $P_2 = 1/\sigma$, considering the freeze-cast materials for the tissue engineering scaffolds application (data comes from Ref. [34]). (BCP: biphasic calcium phosphate, BT: barium titanate).

5. Conclusion

This study developed a predictive PSP model for the freeze-cast porous Si_3N_4-Si_2N_2O ceramic integrating physics-based models and machine learning model from the process-structure-property framework. The interpretable ANN model with SHapley Additive exPlanations advances the systematic understanding of the relationships among the hierarchical microstructural features and their impacts on the mechanical properties, establishing the mathematical design rules for the simultaneous optimization of both mechanical and structural requirements of the freeze-cast porous ceramics.

For the slurry with the same solid loading, the open porosity of freeze-cast scaffolds is governed macroscopically by the sintering parameters. At the first microscopic hierarchical level, the structural wavelength is primarily determined by the freezing conditions; at the second microscopic hierarchical level, the phase transformation and grain growth behavior of the ceramic scaffolds are regulated by the sintering cycles. Thus, four physics-based kinetic equations (including sintering, freezing, phase transformation, and coarsening) are proposed to bridge the process parameters and microstructural features.

Moreover, the R values of ML models derived from the PSP routes are greater than 0.9 both in the train and test sets, exhibiting satisfying predictive and generalization abilities. According to the SHAP analysis, the influence rankings of microstructural features on mechanical properties is: $P>\lambda_{13}>D_{50}>Y$. This model also demonstrates excellent inverse design ability in the validation of two sets of data isolated in advance. Finally, this study demonstrates a PSP model for predicting microstructure and properties of freeze-cast porous ceramics from process parameters by combining physics-based models and interpretable ML, providing a methodological basis for the tuning of freeze-cast ceramics to improve design efficiency. And we believe this physics-based/data driven hybrid modeling path could be applied to the hierarchical design of microstructure and mechanical properties in various freeze-cast porous material cases.

Declaration of interests

The authors declare that they have no known competing financial interests or personal relationships that could have appeared to influence the work reported in this paper.

Acknowledgments

This work was supported by the National Natural Science Foundation of China (Grant No. 51621091, 51972079, and 52072088), the National Key Research and Development Program (Grant No. 2017YFB0310400), and Heilongjiang Touyan Team Program. The authors would like to thank Prof. Suk-Joong L. Kang, Prof. Daqing Wei, Dr. Fan Meng, Dr. Bin Liang, Dr. Fei Zhou, and Dr. Qing Du for their favorable discussion and support.

References

1. L.J. Gibson, M.F. Ashby, Cellular solids: Structure and Properties (2nd ed.), Cambridge University Press, Cambridge (1997)
2. P. Colombo, In praise of pores, Science, 322 (2008), pp. 381-383
3. T. Ohji, M. Fukushima, Macro-porous ceramics: processing and properties, Int. Mater. Rev., 57 (2) (2012), pp. 115-131
4. Y. Chen, N. Wang, O. Ola, Y. Xia, Y. Zhu, Porous ceramics: light in weight but heavy in energy and environment technologies, Mater. Sci. Eng. R-Rep., 143 (2021), Article 100589
5. S. Wu, X. Liu, K.W.K. Yeung, C. Liu, X. Yang, Biomimetic porous scaffolds for bone tissue engineering, Mater. Sci. Eng. R-Rep., 80 (2014), pp. 1-36
6. R.K. Nishihora, P.L. Rachadel, M.G.N. Quadri, D. Hotza, Manufacturing porous ceramic materials by tape casting-a review, J. Eur. Ceram. Soc., 38 (4) (2018), pp. 988-1001
7. L. Wang, L. An, J. Zhao, S. Shimai, X. Mao, J. Zhang, J. Liu, S. Wang, High-strength porous alumina ceramics prepared from stable wet foams, J. Adv. Ceram., 10 (4) (2021), pp. 852-859

8. T. Fukasawa, Z.Y. Deng, M. Ando, T. Ohji, Y. Goto, Pore structure of porous ceramics synthesized from water-based slurry by freeze-dry process, J. Mater. Sci., 36 (10) (2001), pp. 2523-2527
9. T. Fukasawa, M. Ando, T. Ohji, S. Kanzaki, Synthesis of porous ceramics with complex pore structure by freeze-dry processing, J. Am. Ceram. Soc., 84 (1) (2001), pp. 230-232
10. S. Deville, The lure of ice-templating: recent trends and opportunities for porous materials, Scr. Mater., 147 (2018), pp. 119-124
11. G. Shao, D.A.H. Hanaor, X. Shen, A. Gurlo, Freeze casting: from low-dimensional building blocks to aligned porous structures-a review of novel materials, methods, and applications, Adv. Mater., 32 (17) (2020), Article 1907176
12. M. Fukushima, Y. Yoshizawa, T. Ohji, Macroporous ceramics by Gelation-Freezing route using gelatin, Adv. Eng. Mater., 16 (6) (2014), pp. 607-620
13. S. Deville, Freeze-Casting of porous ceramics: a review of current achievements and issues, Adv. Eng. Mater., 10 (3) (2008), pp. 155-169
14. U.G.K. Wegst, M. Schecter, A.E. Donius, P.M. Hunger, Biomaterials by freeze casting, Philos. Trans. R. Soc. A-Math. Phys. Eng. Sci., 368 (2010) (1917), pp. 2099-2121
15. S. Chen, L. Wang, G. He, J. Li, C. Wang, Microstructure and properties of porous Si3N4 ceramics by gelcasting-self-propagating high-temperature synthesis (SHS), J. Adv. Ceram., 11 (1) (2022), pp. 172-183
16. [G. Pezzotti, T. Asai, T. Adachi, E. Ohgitani, T. Yamamoto, N. Kanamura, F. Boschetto, W. Zhu, M. Zanocco, E. Marin, B.S. Bal, B.J. McEntire, K. Makimura, O. Mazda, I. Nishimura, Antifungal activity of polymethyl methacrylate/Si3N4 composites against Candida albicans, Acta Biomater, 126 (2021), pp. 259-276
17. G. Pezzotti, E. Marin, T. Adachi, A. Rondinella, F. Boschetto, W. Zhu, N. Sugano, R.M. Bock, B. McEntire, S.B. Bal, Bioactive silicon nitride: a new therapeutic material for osteoarthropathy, Sci. Rep., 7 (1) (2017), p. 44848
18. Y. Shao, D. Jia, B. Liu, Characterization of porous silicon nitride ceramics by pressureless sintering using fly ash cenosphere as a pore-forming agent, J. Eur. Ceram. Soc., 29 (8) (2009), pp. 1529-1534
19. Y. Zhang, D. Yao, K. Zuo, Y. Xia, J. Yin, H. Liang, Y. Zeng, Effects of N2 pressure and Si particle size on mechanical properties of porous Si3N4 ceramics prepared via SHS, J. Eur. Ceram. Soc., 40 (13) (2020), pp. 4454-4461
20. G. Jiang, J. Yang, Extrusion of highly porous silicon nitride ceramics with bimodal pore structure and improved gas permeability, J. Am. Ceram. Soc., 101 (2) (2018), pp. 520-524
21. T. Ohji, Microstructural design and mechanical properties of porous silicon nitride ceramics, Mater. Sci. Eng. A-Struct. Mater. Prop. Microstruct. Process., 498 (1–2) (2008), pp. 5-11
22. D. Manessis, H.H. Du, R. Larker, Oxide and interface characteristics of oxidized silicon oxynitride ceramics-An investigation by electron microscopy, J. Mater. Sci., 33 (1998), pp. 4447-4453
23. Y.F. Shao, D.C. Jia, Y. Zhou, B.Y. Liu, Novel method for fabrication of silicon nitride/silicon oxynitride composite ceramic foams using fly ash cenosphere as a pore-forming agent, J. Am. Ceram. Soc., 91 (11) (2008), pp. 3781-3785
24. M.F. Ashby, Multi-objective optimization in material design and selection, Acta Mater., 48 (2000), pp. 359-369
25. T. Bligaard, G.H. Jóhannesson, A.V. Ruban, H.L. Skriver, K.W. Jacobsen, J.K. Nørskov, Pareto-optimal alloys, Appl. Phys. Lett., 83 (22) (2003), pp. 4527-4529
26. K.M. Jablonka, G.M. Jothiappan, S. Wang, B. Smit, B. Yoo, Bias free multiobjective active learning for materials design and discovery, Nat. Commun., 12 (1) (2021), p. 2312
27. G.B. Olson, Computational design of hierarchically structured materials, Science, 277 (1997), pp. 1237-1242
28. G.B. Olson, Designing a new material world, Science, 288 (2000), pp. 993-998
29. M.F. Ashby, The properties of foams and lattices, Philos. Trans. R. Soc. A-Math. Phys. Eng. Sci., 364 (1838) (2006), pp. 15-30
30. P.M. Hunger, A.E. Donius, U.G.K. Wegst, Structure-property-processing correlations in freeze-cast composite scaffolds, Acta Biomater., 9 (5) (2013), pp. 6338-6348
31. S. Deville, Freezing colloids: Observations, principles, control, and use: Applications in Materials science, Life science, Earth science, Food science, and Engineering, Springer, Switzerland (2017)
32. S. Deville, E. Saiz, A.P. Tomsia, Freeze casting of hydroxyapatite scaffolds for bone tissue engineering, Biomaterials, 27 (32) (2006), pp. 5480-5489

33. Q.F. Cheng, C.J. Huang, A.P. Tomsia, Freeze casting for assembling bioinspired structural materials, Adv. Mater., 29 (2017), Article 1703155
34. K.L. Scotti, D.C. Dunand, Freeze casting-A review of processing, microstructure and properties via the open data repository, FreezeCasting.net, Prog. Mater. Sci., 94 (2018), pp. 243-305
35. S. Deville, S. Meille, J. Seuba, A meta-analysis of the mechanical properties of ice-templated ceramics and metals, Sci. Technol. Adv. Mat., 16 (4) (2015), Article 043501
36. F. Bouville, E. Maire, S. Deville, Lightweight and stiff cellular ceramic structures by ice templating, J. Mater. Res., 29 (2) (2014), pp. 175-181
37. D. Ghosh, N. Dhavale, M. Banda, H. Kang, A comparison of microstructure and uniaxial compressive response of ice-templated alumina scaffolds fabricated from two different particle sizes, Ceram. Int., 42 (14) (2016), pp. 16138-16147
38. D. Ghosh, H. Kang, M. Banda, V. Kamaha, Influence of anisotropic grains (platelets) on the microstructure and uniaxial compressive response of ice-templated sintered alumina scaffolds, Acta Mater, 125 (2017), pp. 1-14
39. G.L. Hart, T. Mueller, C. Toher, S. Curtarolo, Machine learning for alloys, Nat. Rev. Mater., 6 (8) (2021), pp. 730-755
40. K. Kaufmann, D. Maryanovsky, W.M. Mellor, C. Zhu, A.S. Rosengarten, T.J. Harrington, C. Oses, C. Toher, S. Curtarolo, K.S. Vecchio, Discovery of high-entropy ceramics via machine learning, npj Comput. Mater., 6 (1) (2020), pp. 1-9
41. W.B. Chaabene, M. Flah, M.L. Nehdi, Machine learning prediction of mechanical properties of concrete: critical review, Constr. Build. Mater., 260 (2020), Article 119889
42. S. Lee, J. Lee, B. Hwang, Microstructure-based prediction of yield ratio and uniform elongation in high-strength bainitic steels using multiple linear regression analysis, Mater. Sci. Eng. A-Struct. Mater. Prop. Microstruct. Process., 758 (2019), pp. 56-59
43. C. Wei, L. Gremillard, Towards the prediction of hydrothermal ageing of 3Y-TZP bioceramics from processing parameters, Acta Mater., 144 (2018), pp. 245-256
44. C. Suh, C. Fare, J.A. Warren, E.O. Pyzer-Knapp, Evolving the materials genome: how machine learning is fueling the next generation of materials discovery, Annu. Rev. Mater. Res., 50 (1) (2020), pp. 1-25
45. A. Molkeri, D. Khatamsaz, R. Couperthwaite, J. James, R. Arróyave, D. Allaire, A. Srivastava, On the importance of microstructure information in materials design: PSP vs PP, Acta Mater., 223 (2022), Article 117471
46. K.Y. Yin, K.H. Ji, L.S. Littles, R. Trivedi, A. Karma, U.G.K. Wegst, Hierarchical structure formation by crystal growth-front instabilities during ice templating, Proc. Natl. Acad. Sci. U.S.A., 120 (23) (2023), Article e2210242120
47. S.M. Miller, X. Xiao, K.T. Faber, Freeze-cast alumina pore networks: effects of freezing conditions and dispersion medium, J. Eur. Ceram. Soc., 35 (13) (2015), pp. 3595-3605
48. S.M. Miller, X. Xiao, J.A. Setlock, K.T. Faber, Freeze-cast alumina pore networks: effects of processing parameters in steady-state solidification regimes of aqueous slurries, J. Eur. Ceram. Soc., 38 (15) (2018), pp. 5134-5143
49. D.J. Jeffrey, Conduction through a random suspension of spheres, Proc. R. Soc. A-Math. Phys. Sci., 335 (1602) (1973), pp. 355-367
50. Y.C. Chiew, E.D. Glandt, The effect of structure on the conductivity of a dispersion, J. Colloid Interface Sci., 94 (1) (1983), pp. 90-104
51. M.D. Abràmoff, P.J. Magalhães, S.J. Ram, Image processing with ImageJ, Biophotonics Int., 11 (7) (2004), pp. 36-42
52. M. Banda, D. Ghosh, Effects of porosity and strain rate on the uniaxial compressive response of ice-templated sintered macroporous alumina, Acta Mater., 149 (2018), pp. 179-192
53. K. Hornik, M. Stinchcombe, H. White, Multilayer feedforward networks are universal approximators, Neural Netw., 2 (5) (1989), pp. 359-366
54. J. Nocedal, Updating quasi-Newton matrices with limited storage, Math. Comput., 35 (151) (1980), pp. 773-782
55. S. Lundberg, S. Lee, A unified approach to interpreting model predictions, Adv Neural Inf Process Syst, 30 (2017), pp. 1-10
56. J.S. Weaver, S.R. Kalidindi, U.G.K. Wegst, Structure-processing correlations and mechanical properties in freeze-cast Ti-6Al-4V with highly aligned porosity and a lightweight Ti-6Al-4V-PMMA composite with excellent energy absorption capability, Acta Mater., 132 (2017), pp. 182-192

57. W. Kurz, D.J. Fisher, Fundamentals of Solidification, (3rd ed.), Trans Tech Publications Ltd, Switzerland (1992)
58. A. Vasilios, A.D. Solomon, Mathematical Modeling of Melting and Freezing Processes, Taylor & Francis, Washington (1993)
59. A. Lichtner, D. Roussel, D. Röhrens, D. Jauffres, J. Villanova, C.L. Martin, R.K. Bordia, Anisotropic sintering behavior of freeze-cast ceramics by optical dilatometry and discrete-element simulations, Acta Mater., 155 (2018), pp. 343-349
60. F.L. Riley, Progress in Nitrogen Ceramics, Springer, Netherlands, Dordrecht (1983)
61. E. Munch, E. Saiz, A.P. Tomsia, S. Deville, Architectural control of freeze-cast ceramics through additives and templating, J. Am. Ceram. Soc., 92 (7) (2009), pp. 1534-1539
62. M.M. Porter, R. Imperio, M. Wen, M.A. Meyers, J. McKittrick, Bioinspired scaffolds with varying pore architectures and mechanical properties, Adv. Funct. Mater., 24 (14) (2014), pp. 1978-1987
63. H. Bai, Y. Chen, B. Delattre, A.P. Tomsia, R.O. Ritchie, Bioinspired large-scale aligned porous materials assembled with dual temperature gradients, Sci. Adv., 1 (11) (2015), pp. 1-8
64. J. Seuba, S. Deville, C. Guizard, A.J. Stevenson, The effect of wall thickness distribution on mechanical reliability and strength in unidirectional porous ceramics, Sci. Technol. Adv. Mat., 17 (1) (2016), pp. 128-135
65. A. Lichtner, D. Roussel, D. Jauffrès, C.L. Martin, R.K. Bordia, Effect of macropore anisotropy on the mechanical response of hierarchically porous ceramics, J. Am. Ceram. Soc., 99 (3) (2016), pp. 979-987
66. W.D. Kingery, Densification during sintering in the presence of a liquid phase. I. Theory, J. Appl. Phys., 30 (3) (1959), pp. 301-306
67. W.D. Kingery, M.D. Narasimhan, Densification during sintering in the presence of a liquid phase. II. Experimental, J. Appl. Phys., 30 (3) (1959), pp. 307-310
68. W.D. Kingery, J.M. Woulbroun, F.R. Charvat, Effects of applied pressure on densification during sintering in the presence of a liquid phase, J. Am. Ceram. Soc., 46 (8) (1963), pp. 391-395
69. R.E. Loehman, D.J. Rowcliffe, Sintering of Si3N4-Y2O3-Al2O3, J. Am. Ceram. Soc., 63 (3–4) (1980), pp. 144-148
70. D. Suttor, G.S. Fischman, Densification and sintering kinetics in sintered silicon nitride, J. Am. Ceram. Soc., 75 (5) (1992), pp. 1063-1067
71. O. Abe, Sintering process of Y2O3 and Al2O3-doped Si3N4, J. Mater. Sci., 25 (9) (1990), pp. 4018-4026
72. G.R. Terwilliger, F.F. Lange, Hot-Pressing behavior of Si3N4, J. Am. Ceram. Soc., 57 (1) (1974), pp. 25-29
73. L. Goyos-Ball, E. Fernández, R. Díaz, A. Fernández, C. Prado, R. Torrecillas, E. Saiz, Osseous differentiation on freeze casted 10CeTZP-Al2O3 structures, J. Eur. Ceram. Soc., 37 (15) (2017), pp. 5009-5016
74. S. Flauder, U. Gbureck, F.A. Müller, Structure and mechanical properties of β-TCP scaffolds prepared by ice-templating with preset ice front velocities, Acta Biomater., 10 (12) (2014), pp. 5148-5155
75. M. Avrami, Kinetics of phase change. I general theory, J. Chem. Phys., 7 (12) (1939), pp. 1103-1112
76. K. Barmak, A commentery on: “Reaction Kinetics in Processes of Nucleation and Growth”, Metall. Mater. Trans. A-Phys. Metall. Mater. Sci., 41 (11) (2010), pp. 2711-2775
77. D.A. Porter, K.E. Easterling, M. Sherif, Phase Transformations in Metals and Alloys (3rd ed.), Taylor & Francis Group, Bosa Roca (2009)
78. J.C. Almeida, A.T. Fonseca, R.N. Correia, J.L. Baptista, Pressureless sintering of silicon nitride with additives of the Y2O3-Al2O3-SiO2 system, Mater. Sci. Eng. A-Struct. Mater. Prop. Microstruct. Process., 109 (1989), pp. 395-400
79. A. Bandyopadhyay, S.W. Quander, P.B. Aswath, D.W. Freitag, K.K. Richardson, D.L. Hunn, Kinetics of in-situ α to β Si3N4 transformation in a barium aluminosilicate matrix, Scripta metallurgica et materialia, 32 (9) (1995), pp. 1417-1422
80. S. Ordoñez, I. Iturriza, F. Castro, The influence of amount and type of additives on α→β Si3N4 transformation, J. Mater. Sci., 34 (1) (1999), pp. 147-153
81. L.J. Bowen, R.J. Weston, T.G. Carruthers, R.J. Brook, Hot-pressing and the α-β phase transformation in silicon nitride, J. Mater. Sci., 13 (2) (1978), pp. 341-350
82. G.N. Babini, A. Bellosi, P. Vincenzini, Densification and α-β transformation mechanisms during hot pressing of Si3N4-Y2O3-SiO2 compositions, Mater. Chem. Phys., 11 (4) (1984), pp. 365-400

83. M. Kitayama, K. Hirao, M. Toriyama, S. Kanzaki, Modeling and simulation of grain growth in Si3N4-II. The α-β transformation, Acta Mater., 46 (18) (1998), pp. 6551-6557
84. D. Bucevac, S. Boskovic, B. Matovic, Kinetics of the α-β phase transformation in seeded Si3N4 ceramics, Sci. Sinter., 40 (3) (2008), pp. 263-270
85. I.M. Lifshitz, V.V. Slyozov, The kinetics of precipitation from supersaturated solid solutions, J. Phys. Chem. Solids, 19 (1–2) (1961), pp. 35-50
86. C. Wagner, Theorie der alterung von niederschlägen durch umlösen (Ostwald-reifung), Zeitschrift für Elektrochemie, Berichte der Bunsengesellschaft für physikalische Chemie, 65 (7–8) (1961), pp. 581-591
87. A.J. Ardell, Precipitate coarsening in solids: modern theories, chronic disagreement with experiment, in: Lorimer GW (Eds), Phase transformations '87, the Institute of Metals, London, 1988, pp. 485–494.
88. S. Han, S.-J.L. Kang, Comment on "Kinetics of β-Si3N4 Grain Growth in Si3N4 Ceramics Sintered under High Nitrogen Pressure", J. Am. Ceram. Soc., 76 (12) (1993), pp. 3178-3179
89. M. Kramer, M.J. Hoffmann, G. Petzow, Grain growth studies of silicon nitride dispersed in an oxynitride glass, J. Am. Ceram. Soc., 76 (11) (1993), pp. 2778-2784
90. K. Lai, T. Tien, Kinetics of β-Si3N4 grain growth in Si3N4 ceramics sintered under high nitrogen pressure, J. Am. Ceram. Soc., 76 (1) (1993), pp. 91-96
91. H. Björklund, L.K.L. Falk, K. Rundgren, J. Wasén, β-Si3N4 grain growth, part I: effect of metal oxide sintering additives, J. Eur. Ceram. Soc., 17 (11) (1997), pp. 1285-1299
92. G. Bernard-Granger, R.L. Yeckley, R. L'Amoulen, Densification and grain growth kinetic for silicon nitride, Key Eng. Mater., 132-136 (1997), pp. 892-895
93. R.F. Guo, P.S. Shen, C. Sun, Y.J. Fu, Y.H. Liu, Z.A. Ren, Q.C. Jiang, Effects of composition and sintering temperature on the structure and compressive property of the lamellar Al2O3-ZrO2 scaffolds prepared by freeze casting, J. Mater. Sci., 50 (2015), pp. 5039-5046
94. J.A. Esterhuizen, B.R. Goldsmith, S. Linic, Interpretable machine learning for knowledge generation in heterogeneous catalysis, Nat. Catal., 5 (3) (2022), pp. 175-184
95. G. Kim, H. Diao, C. Lee, A.T. Samaei, T. Phan, M. de Jong, K. An, D. Ma, P.K. Liaw, W. Chen, First-principles and machine learning predictions of elasticity in severely lattice-distorted high-entropy alloys with experimental validation, Acta Mater., 181 (2019), pp. 124-138
96. C. Yang, C. Ren, Y. Jia, G. Wang, M. Li, W. Lu, A machine learning-based alloy design system to facilitate the rational design of high entropy alloys with enhanced hardness, Acta Mater., 222 (2022), Article 117431
97. M. Zaki, V. Venugopal, R. Bhattoo, S. Bishnoi, S.K. Singh, A.R. Allu, N.M.A.Krishnan Jayadeva, Interpreting the optical properties of oxide glasses with machine learning and Shapely additive explanations, J. Am. Ceram. Soc., 105 (6) (2022), pp. 4046-4057
98. E. Ryshkewitch, Compression strength of porous sintered alumina and zirconia, J. Am. Ceram. Soc., 36 (2) (1953), pp. 65-68
99. R.L. Coble, W.D. Kingery, Effect of porosity on physical properties of sintered alumina, J. Am. Ceram. Soc., 39 (11) (1956), pp. 377-385
100. Ö. Keleş, R.E. García, K.J. Bowman, Stochastic failure of isotropic, brittle materials with uniform porosity, Acta Mater., 61 (8) (2013), pp. 2853-2862

Appendix. Supplementary materials

The custom-made freeze-casting system and in-situ temperature profiles

The schematic of the custom-made freeze-casting system is illustrated in Fig. S 1. The slurries are frozen after pouring into a PTFE mould (39 mm side length, 60 mm height) placed at the top of the copper cold finger. The copper cold finger is cooled by a liquid nitrogen bath and the temperature (i.e. freezing temperature T_{cold}) of its top surface is controlled by a band heater and a thermocouple.

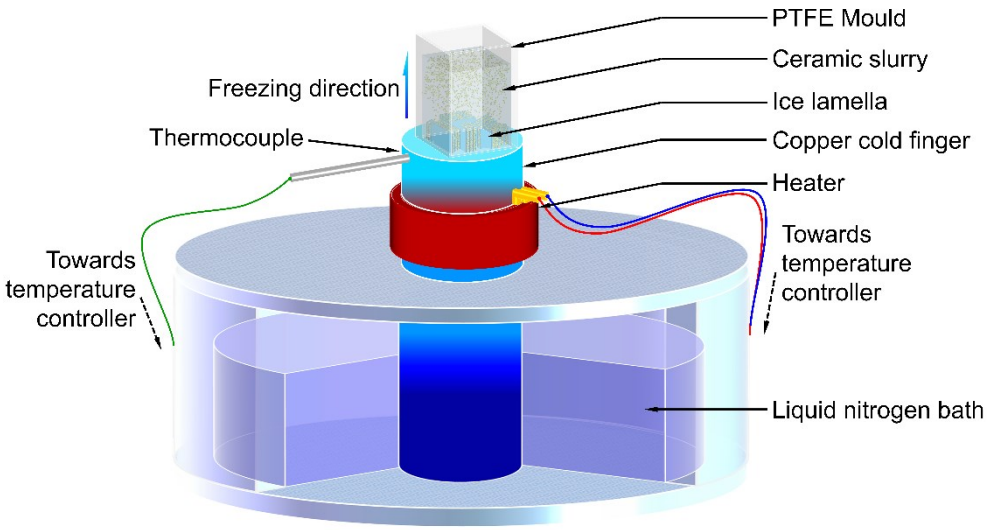

Fig. S 1 The schematic of the custom-made freeze-casting system

The position Z and velocity V of the freezing front,
along with their corresponding regression fits, are measured within a "thermocouple" mould. Fig. S 2 depicts the results for T_{cold} = -40 °C, -60 °C, and -80 °C, respectively.

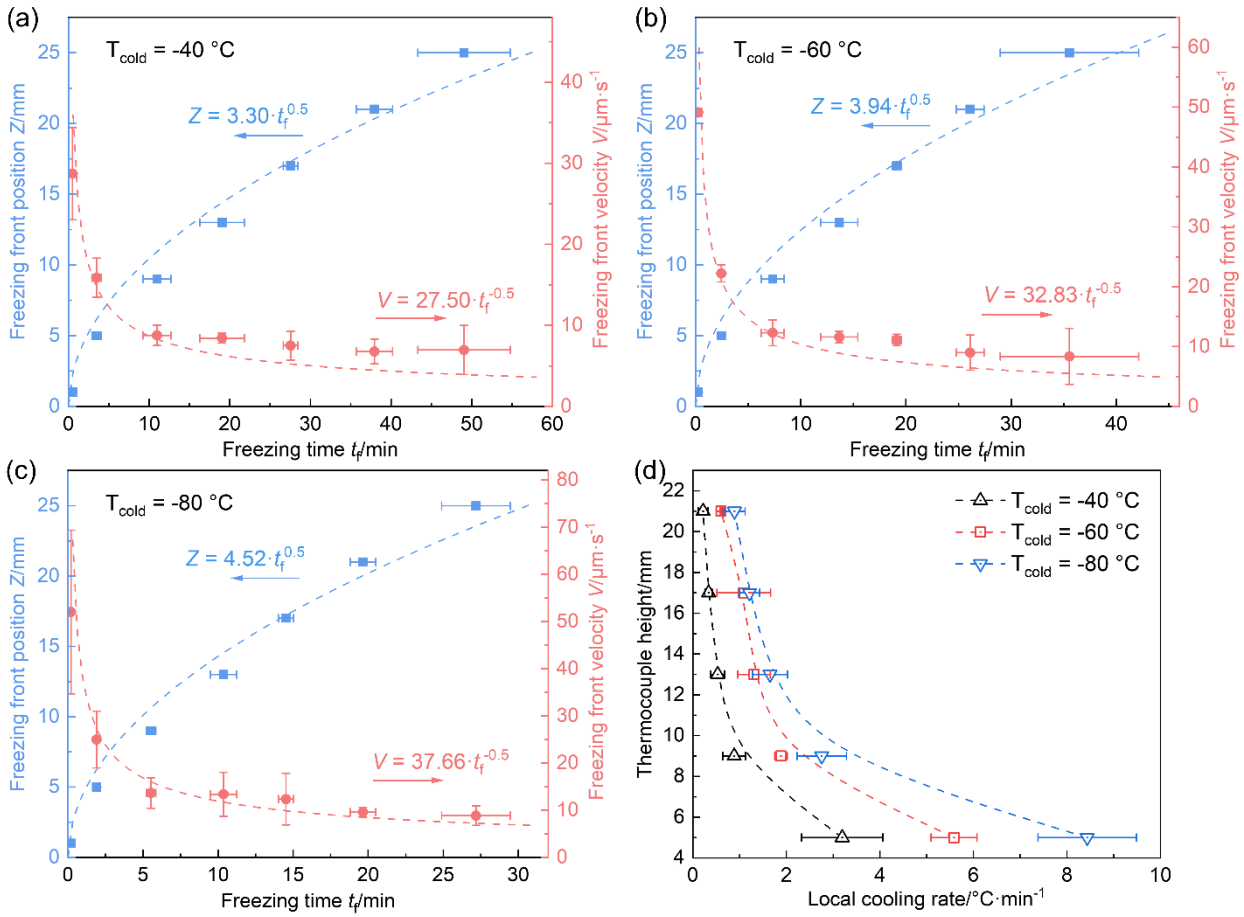

Fig. S 2 The measured and fitted position Z and velocity V of the FF during freeze-casting at (a) -40 °C, (b) -60 °C and (c) -80 °C, and (d) their local cooling rates along the height.

Thermophysical properties of solid particles, dispersion media, slurry, and frozen solid

Thermal and physical properties of solid particles and dispersion media are obtained from the literature, as shown in Table S 1and Table S 2, respectively. Since the amount of water is 80 vol.% of total slurry, we take the temperature-dependent thermal and physical properties of water into account for the two-phase Stefan problem, while ignoring the variation of that of solid particles in the range of 25°C to -100°C. Specifically, the thermophysical properties of water and solid particles at 25 °C and hexagonal ice at -100 °C are used as initial parameters for the calculation of that of slurry and frozen solid. And the calculated thermophysical property values are also listed in Table S 2.

Table S 1 Thermophysical properties of solid particles

Properties (25 ℃)	Si_3N_4	Fused SiO_2	Al_2O_3	Y_2O_3
ρ, g/cm^3	3.184	2.190	3.980	5.010
c_p, J/g·K	0.70[1]	0.70[1]	0.88[1]	0.45[2]
k, W/m·K	35[1]	1.7[1]	25[1]	14[1]

Table S 2 Thermophysical properties of dispersion media and slurry

Thermophysical properties	Liquid state (T_{hot}=25 ℃)	Solid state (T_{cold}=-100 ℃)
For H_2O		
T_m, ℃	0[3]	0[3]
ρ_{H_2O}, g/cm^3	0.997[4]	0.929[3]
c_{pH_2O}, J/g·K	4.18[4]	1.38[3]
k_{H_2O}, W/m·K	0.61[4]	3.69[3]
L_{H_2O}, J/g	333.4[3]	333.4[3]
For slurry		
ρ_{slurry}, g/cm^3	1.421	1.342
$c_{pslurry}$, J/g·K	2.69	1.09
k_{slurry}, W/m·K	1.04	8.67
L_{slurry}, J/g	187.2	187.2

Mechanical cutting of freeze-cast scaffolds for the structural characterization

For the measurement of structural feature size (including pore size p, wall thickness w, and structural wavelength λ), each freeze-cast scaffold was first cut into cubes with a side length of ~6 mm, and then the cubes were cut at 5 mm, 7 mm, 9 mm, 11 mm, and 13 mm from the bottom, as shown in Fig. S 3. The height of feature size measurement from the bottom is indicated by the subscript number (e.g. p_{13} means the pore size measured at 13 mm from the bottom).

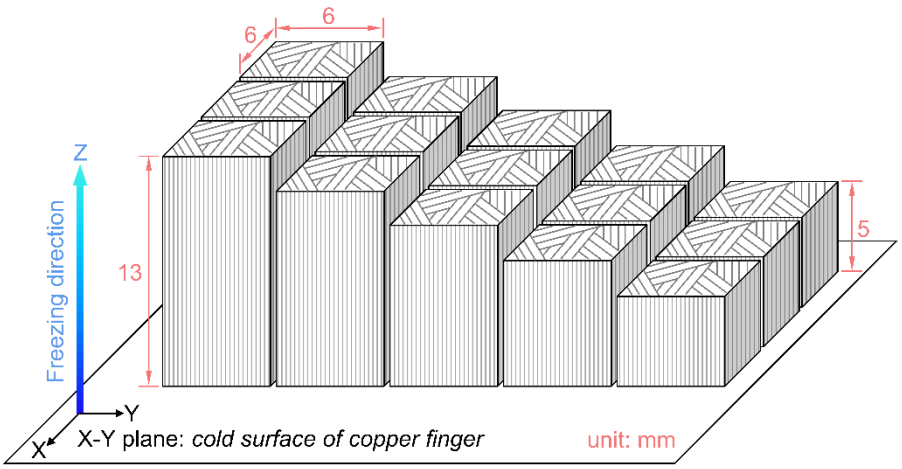

Fig. S 3 Schematic of the mechanical cutting of samples for the structural characterization

Pore size distribution of typical freeze-cast scaffolds and structural analysis of green body

The pore size distributions (at ~13 mm) of typical freeze-cast scaffolds, fabricated under various processing conditions, are evaluated using mercury intrusion porosimetry, as shown in Fig. S 4.

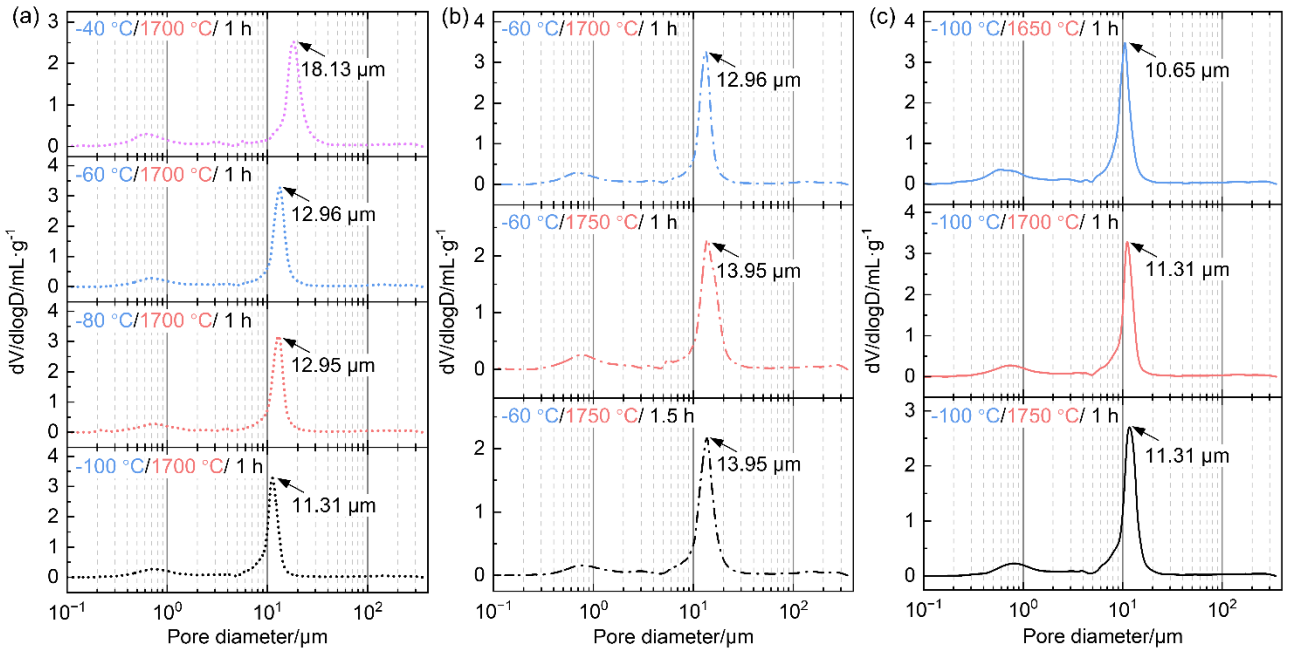

Fig. S 4 Pore size distribution of freeze-cast scaffolds prepared under various processing parameters: (a) different T_{cold}, (b) and (c) different sintering parameters.

Fig. S 5 presents the statistical measurements of microstructural feature sizes at 16.9 mm and 13.9 mm (i.e. at 13 mm of the sintered scaffolds) of the green body freeze-casting at -40 °C and -100 °C, respectively.

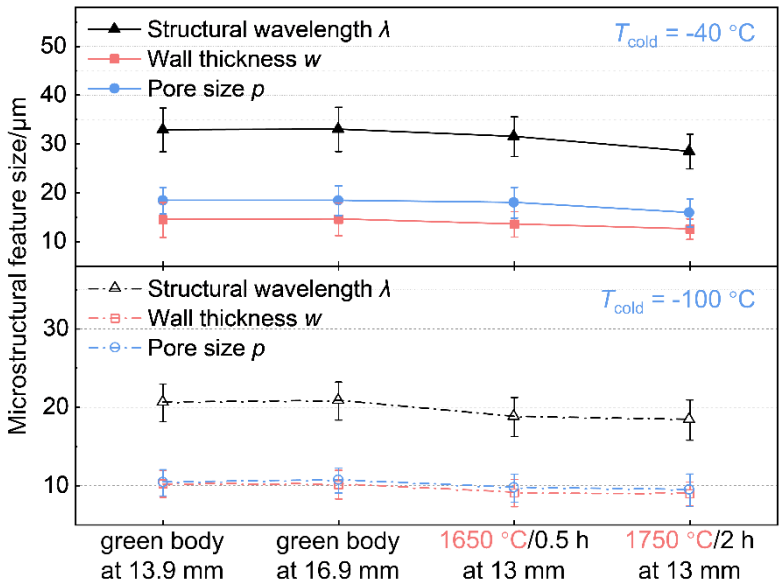

Fig. S 5 Microstructural feature size of green body and typical sintered scaffolds.

XRD Rietveld refinements

The phase content of samples prepared under different sintering parameters was identified by the Rietveld refinement of X-ray diffraction pattern with the open-source FullProf suite software. Two representative XRD Rietveld refinements was given in Fig. S 6.

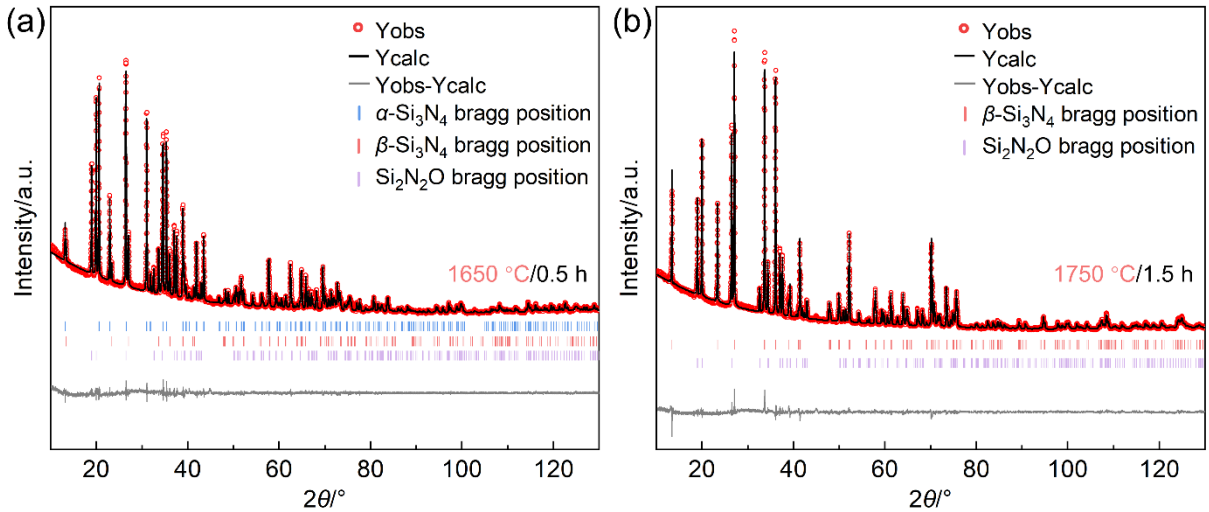

Fig. S 6 The representative XRD Rietveld refinements of samples sintered at (a) 1650 °C/0.5 h, (b) 1750 °C/1.5 h.

Prediction of mechanical properties in a traditional process-property (PP) black-box model

According to the traditional microstructure-agnostic artificial neural network (ANN) approach, three process parameters (freezing temperature T_{cold}, sintering temperature T_s and holding time t_s) as feature descriptors are used as inputs to this PP model. And the compressive strength is used as the output to this PP model.

Fig. S 7(a) and (b) shows the predicted and observed compressive strength in the train set and test set from the PP model, respectively, indicating that the PP and PSP models have the similar level of accuracy. The compressive strength heatmap predicted by the PP model in Fig. S 7(c) draws a similar trend consistent with that by the PSP model. And the corresponding predicted σ_{max} reach 40.7 MPa in the PP model. The feature importance calculated by SHAP analysis for the PP model is demonstrated in Fig. S 7(d), elucidating that the influence rankings of process parameters on mechanical properties is t_s>T_s>T_{cold}. And the influence of sintering process parameters on mechanical properties is slightly stronger than that of freezing temperature (the maximum difference in global SHAP value is only 0.443).

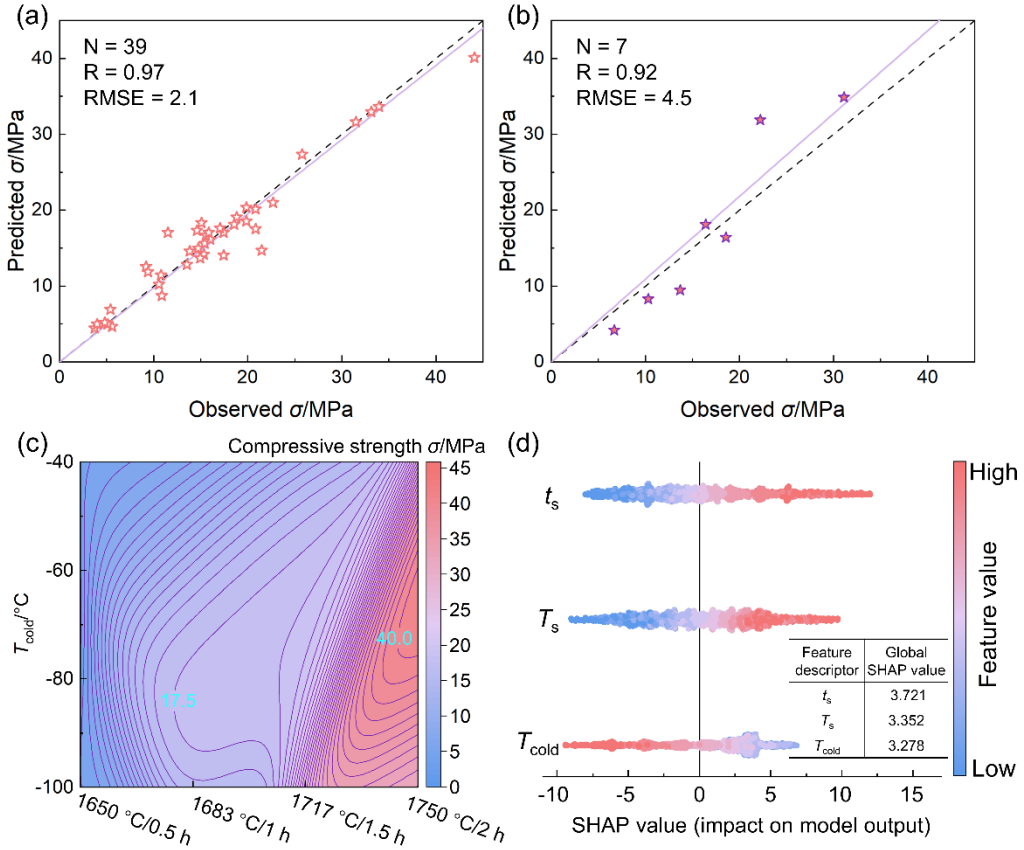

Fig. S 7 The predicted compressive strength σ as a function of the observed σ for (a) the train set and (b) the test set of the PP model, respectively. (c) Compressive strength heatmap predicted from the PP model (The x-axis of the heatmaps physically represents the combination of sintering parameters that fall on the diagonal line of sintering temperature and holding time). (d) The feature descriptors' importance ranking from the SHAP analysis of the PP model.

References

[1] MatWeb and Databases. Available at: https://www.matweb.com/.
[2] Section 5: Thermochemistry, Electrochemistry, and Solution Chemistry, in: W.H. Haynes (Editor-in-Chief), CRC Handbook of Chemistry and Physics (97th ed.), CRC Press/Taylor and Francis, Boca Raton, Florida, 2016, pp. 42.
[3] A.H. Harvey. Properties of ice and supercooled water, in: W.H. Haynes (Editor-in-Chief), CRC Handbook of Chemistry and Physics (97th ed.), CRC Press/Taylor and Francis, Boca Raton, Florida, 2016.
[4] E.W. Lemmon, M.O. McLinden, D.G. Friend. Thermophysical properties of fluid systems, in: P.J. Linstrom, W.G. Mallard (Editors), NIST Chemistry WebBook, NIST standard reference database 69. National Institute of Standards and Technology, 2021.